Water mass transformation and the North Atlantic Current in three multicentury climate model simulations

H. R. Langehaug,[1,2] P. B. Rhines,[3] T. Eldevik,[2,4] J. Mignot,[5] and K. Lohmann[6]

Received 6 March 2012; revised 15 September 2012; accepted 17 September 2012; published 2 November 2012.

[1] The warm and saline Subtropical Water carried by the North Atlantic Current undergoes substantial transformation on its way to higher latitudes, predominantly from oceanic heat loss to the atmosphere. The geographical distribution of the surface forced water mass transformation is assessed in multicentury climate simulations from three different climate models (BCM, IPSLCM4, and MPI-M ESM), with a particular focus on the eastern subpolar North Atlantic Ocean. A diagnosis, originally introduced by Walin (1982), estimates the surface water mass transformation from buoyancy forcing. While the depth structure of the Atlantic Meridional Overturning Circulation (AMOC) is similar in all models, their climatological heat and freshwater fluxes are very different. Consistently, the models differ in their mean pathways of the North Atlantic Current, location of upper ocean low salinity waters, as well as in sea ice cover. In the two models with an excessive sea ice extent in the Labrador Sea, most of the water mass transformation in the subpolar region occurs in the eastern part (east of 35°W). The variability of the eastern water mass transformation on decadal time scales is related to the variable warm northward flow into the subpolar region, the upper branch of AMOC, where a strengthened flow leads an intensified transformation. This relationship seems to disappear with a weak connection between the Subtropical and Subpolar gyres.

Citation: Langehaug, H. R., P. B. Rhines, T. Eldevik, J. Mignot, and K. Lohmann (2012), Water mass transformation and the North Atlantic Current in three multicentury climate model simulations, *J. Geophys. Res.*, *117*, C11001, doi:10.1029/2012JC008021.

1. Introduction

[2] The North Atlantic Current carries warm and saline Subtropical Water northward to the eastern subpolar region (Figure 1a). This flow therefore transports large amounts of heat and salt poleward. The associated heat loss to the (sub-) polar atmosphere contributes to the relatively warm European climate, both on annual and seasonal timescales [*Rahmstorf*, 2002; *Rhines et al.*, 2008]. When Subtropical Water is cooled and freshened on its way northward, it results in a *transformation* of Subtropical Water to colder and fresher Subpolar Mode Water (Figure 1b) [*Pérez-Brunius et al.*, 2004; *Brambilla et al.*, 2008]. In the subtropics Subtropical water is mainly transformed due to cooling [*Old and Haines*, 2006], whereas farther north Subtropical Water is also transformed by discharge of seasonal Arctic sea ice melt, river run-off, and precipitation [e.g., *Isachsen et al.*, 2007]. Hence, the transformation of Subtropical Water links directly to the operation of the coupled atmosphere-ocean climate system. For instance, identifying the location and strength of the model transformation maps out where the ocean potentially influences the atmosphere the most.

[3] The first and main objective of this study is to compare thermodynamic, surface forced *water mass transformation* (hereafter denoted WMT) in the northern North Atlantic in three different climate model simulations, and to address why they differ. *Carman and McClean* [2011] showed that WMT in the North Atlantic Ocean is very model dependent over a suite of IPCC AR4 climate models. This model divergence underlines the importance of assessing climate model WMT in the North Atlantic Ocean, and more fundamentally, identifying *why* models differ. Whereas *Carman and McClean* [2011] were concerned with simulations of 20th century climate, our focus is the WMT in multicentury simulations of pre-industrial climates. These long-term control simulations allow us to investigate climate variability on decadal timescales, and in particular to quantify decadal variance of WMT in the eastern subpolar region. Observed hydrographic properties in the eastern subpolar region are in general associated with large (multi)decadal variability [e.g., *Reverdin*, 2010].

[4] An extensive analysis on observation-based WMT in the eastern subpolar region was done by *Brambilla et al.* [2008].

[1]Nansen Environmental and Remote Sensing Center, Bergen, Norway.
[2]Bjerknes Centre for Climate Research, Bergen, Norway.
[3]School of Oceanography, University of Washington, Seattle, Washington, USA.
[4]Geophysical Institute, University of Bergen, Bergen, Norway.
[5]LOCEAN, Institute Pierre Simon Laplace, University Pierre and Marie Curie, Paris, France.
[6]Max Planck Institute for Meteorology, Hamburg, Germany.

Corresponding author: H. R. Langehaug, Nansen Environmental and Remote Sensing Center, Thormøhlensgate 47, NO-5006 Bergen, Norway. (helene.langehaug@nersc.no)

0148-0227/12/2012JC008021

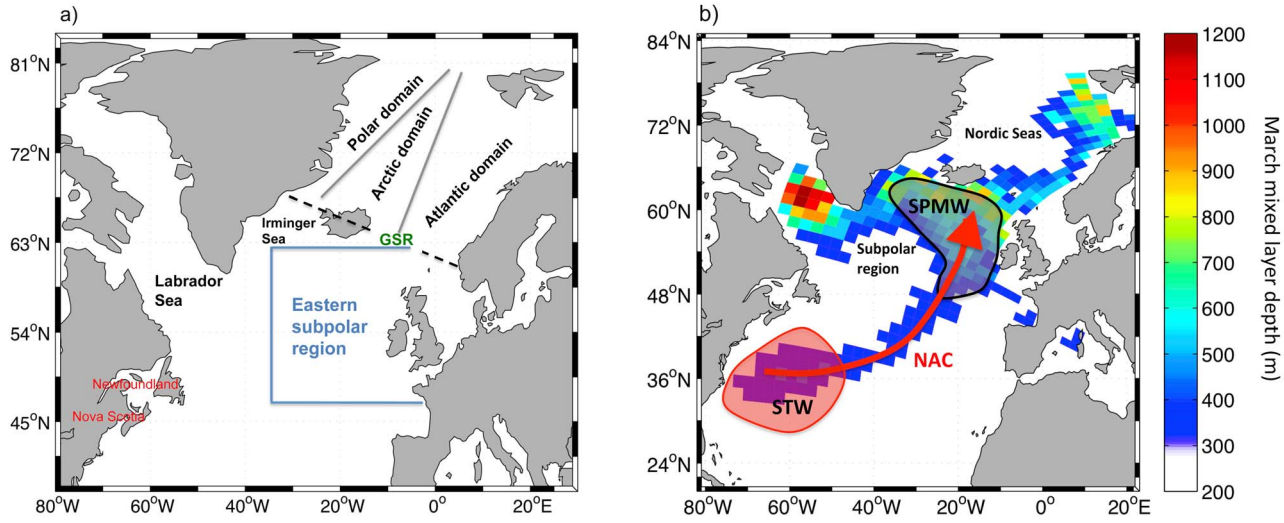

Figure 1. (a) Map of the Subpolar North Atlantic and the Nordic Seas with names of geographical regions that are referred to in the text. The eastern subpolar region is indicated by the blue lines, and the rest of the subpolar region is the western subpolar region. The Nordic Seas are divided into three domains [after *Swift*, 1986]. The location of the Greenland-Scotland Ridge (GSR) is indicated with the dashed black line. (b) Schematics of the transformation of Subtropical Water (STW) to Subpolar Mode Water (SPMW) along the pathway of the North Atlantic Current (NAC). The mixed layer depth shown in color is the mean mixed layer depth in March over 500 years (obtained from the Bergen Climate Model). The mean mixed layer depth is deepest in March.

Areas of strong WMT are associated with deep mixed layers and formation of Subpolar Mode Water, which is the dominant water mass above the permanent pycnocline in the eastern subpolar region [*McCartney and Talley*, 1982; *Brambilla and Talley*, 2008]. Subpolar Mode Water is associated with branches of the North Atlantic Current and each branch becomes denser along its path [*Brambilla and Talley*, 2008, Figure 1]. Some branches enter the Nordic Seas and others re-circulate within the subpolar region. The net transport of the North Atlantic Current in the subpolar region has rather widely varying estimates, for example, 12 Sv [*Schmitz and McCartney*, 1993], whereas *Rossby* [1996] estimates 20 Sv for the North Atlantic Current passing through the Charlie-Gibbs Fracture Zone. Strong eddies and re-circulations complicate these estimates, as does the vertical range over which the estimates apply. The northward transport across the Greenland-Scotland Ridge is about 9 Sv [*Østerhus et al.*, 2005]. This indicates that about half of the North Atlantic Current is continuing to the Nordic Seas and the other half re-circulates in the subpolar region. The fraction of the westward (toward the Labrador Sea) and poleward branch of the North Atlantic Current is important in determining the water mass composition of the dense North Atlantic Deep Water, in particular the Deep Western Boundary Current [*Smethie and Fine*, 2001; *Lumpkin and Speer*, 2003].

[5] The North Atlantic Current forms the upper branch of the Atlantic Meridional Overturning Circulation (AMOC) [e.g., *Manabe and Stouffer*, 1988]. The variable strength of this zonally integrated circulation has been investigated in a range of numerical models [e.g., *Bentsen et al.*, 2004; *Jungclaus et al.*, 2005; *Medhaug et al.*, 2012]. AMOC is traditionally quantified in latitude-depth space (hereafter denoted AMOCz). In the present study—where we analyze WMT—it is more appropriate to quantify the overturning in latitude-density space (AMOCσ) [e.g., *Mauritzen and Häkkinen*, 1999; *Bailey et al.*, 2005]. AMOCσ illustrates the density distribution that corresponds to the zonally integrated volume transport. Density changes associated with the North Atlantic Current, for instance, are therefore evident in AMOCσ. Due to strong zonal density gradients, AMOCσ differs greatly from AMOCz in the subpolar region [*Willebrand et al.*, 2001; *Zhang*, 2010]. Note that changes in water mass properties are possible without density changes, for instance, when salinity and temperature changes are density compensated.

[6] The second objective of this study is to investigate the relationship between model WMT in the eastern subpolar region and AMOCσ variability on decadal timescales. Several studies have investigated the relationship between AMOC and WMT at high northern latitudes [e.g., *Marsh*, 2000; *Isachsen et al.*, 2007; *Grist et al.*, 2009; *Josey et al.*, 2009]. *Josey et al.* [2009] found that the integrated WMT from air-sea exchange north of 35°N relates strongly with the strength of AMOCz between 35°N and 65°N. The other source for WMT is mixing, such as lateral mixing within the mixed layer, entrainment of denser water into the mixed layer, and diapycnal mixing [*Nurser et al.*, 1999]. Estimates for the North Atlantic suggest that mixed layer entrainment is significant, yet not dominating the WMT, and often opposes the surface forced WMT [*Tandon and Zhao*, 2004]. Diapycnal mixing plays an important role in the WMT of dense Nordic Seas overflow water passing through the Denmark Strait, Faroe-Bank Channel, and Iceland-Faroe Ridge [e.g., *Dickson and Brown*, 1994; *Hansen and Østerhus*, 2000], and in the subsequent rising of deep water masses throughout the world ocean.

[7] The focus of our study is the WMT associated with the North Atlantic Current in the upper ocean, and we accordingly only consider WMT due to surface forcing. Previous studies have shown that WMT at high northern latitudes is dominated by air-sea exchanges [*Nurser et al.*, 1999; *Tandon and Zhao*, 2004]. *Nurser et al.* [1999] used an isopycnal model to investigate the contribution from mixing and air-sea exchanges on the total WMT in the North Atlantic Ocean. They found that WMT could be calculated to first order from surface forcing only outside the Tropics. This is corroborated by the observation-based study of *Lumpkin and Speer* [2003], which point out that air-sea exchanges dominate *south* of the overflow region downstream of the Greenland-Scotland Ridge. *Pérez-Brunius et al.* [2004] distinguish between the WMT in the western and eastern subpolar region. They found that water entering the Labrador Sea is mainly transformed by mixing with fresh and cold subpolar waters. In the eastern region, the focus region in this study, the main factors in transforming Subtropical Water are air-sea exchanges and horizontal entrainment of saline water from the northeastern subtropical gyre. The entrainment of saline water is not explicitly investigated in this study. However, this entrainment influences the surface density, and thus implicitly contributes to the WMT assessed herein.

[8] The paper is organized as follows. The three climate models and the methods used are presented in section 2. In section 3, the models' surface forced WMT is presented, and in section 4 we discuss *why* the models are different from each other, and also why they differ from the observation-based WMT. In section 5, the surface forced WMT in the eastern subpolar region is related to the strength of AMOCσ on decadal timescales. The main conclusions from the study follow in section 6.

2. Data and Method

2.1. Model Descriptions

[9] Multicentury simulations from three different climate models are compared in the present study: the Bergen Climate Model (BCM) [*Furevik et al.*, 2003; *Otterå et al.*, 2009], the Institute Pierre Simon Laplace Coupled Model (IPSLCM4) [*Marti et al.*, 2010; *Servonnat et al.*, 2010], and the Max Planck Institute for Meteorology Earth System Model (MPI-M ESM) [*Jungclaus et al.*, 2010]. We use the control simulations from the EU project THOR (Thermohaline Overturning – at Risk?), and the first 500 years following model spin-up are investigated. All models are run without flux adjustments and are thus free to evolve following their own climates. The multicentury simulations allow for robust investigation of long-term climatologies and (multi)decadal variability. The model resolutions are accordingly relative coarse compared, e.g., to 20th century climate simulations. The three climate models of very different constructions are widely used by the climate research community. It is accordingly pertinent to investigate how – and how well – they simulate the North Atlantic climate.

[10] The ocean model used in the BCM is MICOM (Miami Isopycnic Coordinate Ocean Model) [*Bleck et al.*, 1992], which has a horizontal grid spacing of approximately 2.4° × 2.4° (lon × lat), except in the equatorial region. There are 34 isopycnic layers in the vertical; the potential densities range from σ_2 = 1031.51 to σ_2 = 1037.80 kg m^{-3} (globally), and a non-isopycnic surface mixed layer provides the linkage between the atmospheric forcing and the ocean interior. Three processes determine the mass exchange across the interface between the mixed layer and the isopycnic layers: (1) mixing across the interface, (2) mass exchange caused by changes in mixed layer depth, and (3) convective adjustment. Whenever the water column becomes statically unstable, e.g., in the Labrador or Irminger seas, there is an instantaneous re-stratification of the water column where dense water in the mixed layer is transferred to the corresponding isopycnic layer below [*Medhaug et al.*, 2012]. The thermodynamic-dynamic sea ice model used in BCM is GELATO (Global Experimental Leads and sea ice for Atmosphere and Ocean) [*Salas Mélia*, 2002], a multicategory sea-ice model (thickness dependent), with one layer for snow and four layers for ice. The atmosphere model is run with a truncation at wave number 63 (T_L63) with 31 vertical levels. The horizontal grid spacing is about 2.8° in longitude and latitude. The model data are taken from a 700-year control integration based on pre-industrial climate and has previously been used in several climate studies [*Otterå et al.*, 2009; *Langehaug et al.*, 2012; *Medhaug et al.*, 2012].

[11] BCM is too warm in the North Atlantic subpolar region compared to observations, whereas the biases are relatively small in sea surface salinity [*Otterå et al.*, 2009]. Perhaps due to the warm bias, the winter sea ice extent is too small in the Labrador Sea compared to observations [*Otterå et al.*, 2009]. The deep convection in this model is fairly realistic, where dense water is formed at the eastern rim of the Nordic Seas, close to the Greenland-Scotland Ridge, and in the Irminger and Labrador seas. The contribution from the Nordic Seas and Labrador Sea, constitute 2/3 and 1/3, respectively, of the deep water in the North Atlantic Basin [*Medhaug et al.*, 2012].

[12] OPA8 (Océan PArallélisé) [*Madec et al.*, 1997], the ocean model used in IPSLCM4, has 31 vertical depth levels and a nominal 2°-horizontal resolution. To parameterize ocean convection, the vertical eddy viscosity and diffusivity coefficients are increased to 100 m^2 s^{-1} in case of static instability. The sea ice model is the LIM-2 (Louvain-la-Neuve sea Ice Model) thermodynamic–dynamic sea ice module specifically designed for climate studies [*Fichefet and Morales-Maqueda*, 1997, 1999]. It includes one layer for snow and two layers for ice. The atmosphere model has a horizontal resolution of 3.75° × 2.535° and 19 vertical levels. The model data is taken from a 1000-year control integration based on pre-industrial climate and has been used in several climate studies [*Servonnat et al.*, 2010; *Gastineau and Frankignoul*, 2011].

[13] IPSLCM4 is colder than observations over the whole North Atlantic Ocean [*Escudier et al.*, 2012]. In particular, a very large cold bias is present east of the Grand Banks. This is in part due to a southward shift of the western boundary currents as in many other models [e.g., *Danabasoglu*, 2008]. A strong negative bias in sea surface salinity is present in the northwestern Atlantic, linked to an excess of freshwater forcing over the Labrador Sea, as in the previous version of the model [*Swingedouw et al.*, 2007]. Together with the temperature bias discussed above, this cold and fresh bias is associated with an overestimation of the winter sea ice cover in the Labrador Sea. This prevents a correct representation of deep convection in this area. Deep convection is nevertheless found in three distinct sites: the Nordic Seas, the southern tip of Greenland at the entrance of the Labrador Sea, and an area

located south of Iceland [*Marti et al.*, 2010; *Escudier et al.*, 2012].

[14] The MPI-M ESM ocean component, MPI-OM (Max Planck Institute Ocean Model) [*Marsland et al.*, 2003], applies a conformal mapping grid with a horizontal resolution ranging from 20 km to 350 km and 40 vertical depth levels. The North Pole of the grid is located over Greenland resulting in a horizontal resolution of 20 to 150 km in the North Atlantic. The convective adjustment scheme used in the ocean model is the parameterization of convection by enhanced vertical diffusion (from 10^{-5} m^2s^{-1} to 10^{-1} m^2s^{-1}) in the presence of static instability. Compared to IPSLCM4 the diffusion coefficient is small, meaning that it takes more time steps to remove the instability. Sea ice dynamics and thermodynamics are embedded in the ocean model and are described in detail in *Marsland et al.* [2003]. The atmosphere model is run with T31 resolution and 19 vertical levels. The model data is taken from a 3000-year control integration based on a pre-industrial climate [*Jungclaus et al.*, 2010].

[15] In MPI-M ESM the simulated path of the North Atlantic Current has a rather zonal direction, crossing the entire North Atlantic Basin before flowing northward along the eastern rim of the basin, as is also discussed in section 4.2. Therefore MPI-M ESM tends to be too cold and fresh in the subpolar North Atlantic compared to observations. The bias in sea surface temperature reaches more than 1 Kelvin as is discussed in *Jungclaus et al.* [2006] for a higher resolution grid configuration than the one used here. Deep water formation in MPI-M ESM occurs in the eastern part of the Nordic Seas as well as south of Greenland [e.g., *Zhu and Jungclaus*, 2008].

[16] The freshwater flux (Q_F) is implemented differently in the three models: In BCM, it is represented by the equivalent virtual salt flux (Q_S), thus neglecting the volume change associated with freshwater input. The virtual salt flux includes all freshwater sources: evaporation (E), precipitation (P), and contributions from river runoff (R) and sea ice melting/freezing. The freshwater flux for IPSLCM4 also includes all sources, and the free surface formulation of *Roullet and Madec* [2000] is applied in this model. MPI-M ESM uses a semi-implicit free surface scheme [*Marsland et al.*, 2003]. For the MPI-M ESM integration presented in this study, the surface fresh water flux output contains only the atmospheric part (i.e., $P\text{-}E + R$). The freezing and melting of sea ice is internal to the model ocean, and unfortunately not part of online diagnostics; it cannot adequately be reconstructed offline based on model output [*Marsland et al.*, 2003].

2.2. Observation-Based and Reanalysis Surface Fluxes

[17] The heat and freshwater fluxes from the models are compared with observation-based estimates and reanalysis, respectively. The latter is provided by the very commonly used NCEP reanalysis product [*Kalnay et al.*, 1996]. The freshwater fluxes are estimated from monthly precipitation, evaporation, and river runoff for the 1948 to 2010 period. Any contribution from sea ice melting/freezing is not included in the reanalysis. This contribution is therefore subtracted from the freshwater fluxes in BCM and IPSLCM4 when comparing models with NCEP. It is important to note that reanalysis surface fluxes can contain large uncertainties [e.g., *Röske*, 2006; *Large and Yeager*, 2009]. This is particularly the case for freshwater fluxes from NCEP [*Béranger et al.*, 2006]. In this study we only use the long-term annual mean of both reanalysis freshwater fluxes and observation-based heat fluxes.

[18] Heat fluxes are provided by the National Oceanography Centre, Southampton (NOC1.1a) [*Josey et al.*, 1999; *Grist and Josey*, 2003]. This data set is based on ship data from the period 1980 to 1993, and we have thus prioritized observation-based data when available at the expense of having one reference data source. The data set is further more an updated version of what was used in the WMT study by *Brambilla et al.* [2008]. The ocean heat budget of this data set is balanced with an accuracy of 2 W m^{-2} using inverse analysis [*Grist and Josey*, 2003], and the data set is distributed as a monthly climatology. (NOC1 was previously referred to as the Southampton Oceanography Centre (SOC) flux climatology.)

2.3. Water Mass Transformation Diagnosed From Surface Buoyancy Fluxes

[19] The quantification of surface forced WMT follows the method that was introduced by *Walin* [1982] and further developed by *Speer and Tziperman* [1992]. The approach is based on the fact that surface heat and freshwater fluxes modify the temperature and salinity at the ocean's surface and thereby convert water from one density class to another – unless the two fluxes are perfectly density-compensated. *Walin* [1982] and *Speer and Tziperman* [1992] showed that the WMT of surface waters in an outcrop region due to air-sea exchanges is equivalent to the volume transport across the outcropping isopycnal in a steady state. This study is concerned with surface forced WMT as argued above. This means that density changes due to cooling/heating of the ocean surface, evaporation, precipitation, and contributions from river runoff and ice melting/freezing are taken into account. Density changes due to interior mixing between different water masses, on the other hand, are neglected. The surface forced WMT is estimated from monthly data.

[20] The surface density flux D (kg m^{-2} s^{-1}) quantifies the local rate of surface WMT, which includes surface heat flux Q_H (W m^{-2}) and freshwater flux Q_F (kg m^{-2} s^{-1}) into the ocean, as well as surface salinity S (dimensionless). The density flux has one thermal (F_T) and one haline (F_S) component:

$$D = F_T + F_S \tag{1}$$

$$F_T = \alpha {c_w}^{-1} Q_H \tag{2}$$

$$F_S = -\beta S \times Q_F \tag{3}$$

where c_w is specific heat capacity of water (3996 J kg^{-1} K^{-1}), and α and β are the thermal expansion coefficient and haline contraction coefficient, respectively. We have here used the UNESCO formulas [*McDougall*, 1987] to calculate α and β.

[21] The surface forced water mass transformation F is equal to a volume transport across the given isopycnal (i.e., diapycnal transport), and is given by integrating the surface density flux over the outcrop region for surface densities between σ and $\sigma + \Delta\sigma$ (Figure 2a) [*Speer and Tziperman*, 1992]:

$$F(\sigma) = \lim_{\Delta\sigma \to 0} \frac{1}{\Delta\sigma} \int_{\sigma}^{\sigma+\Delta\sigma} D \; dA \tag{4}$$

where A is the area of the outcrop region.

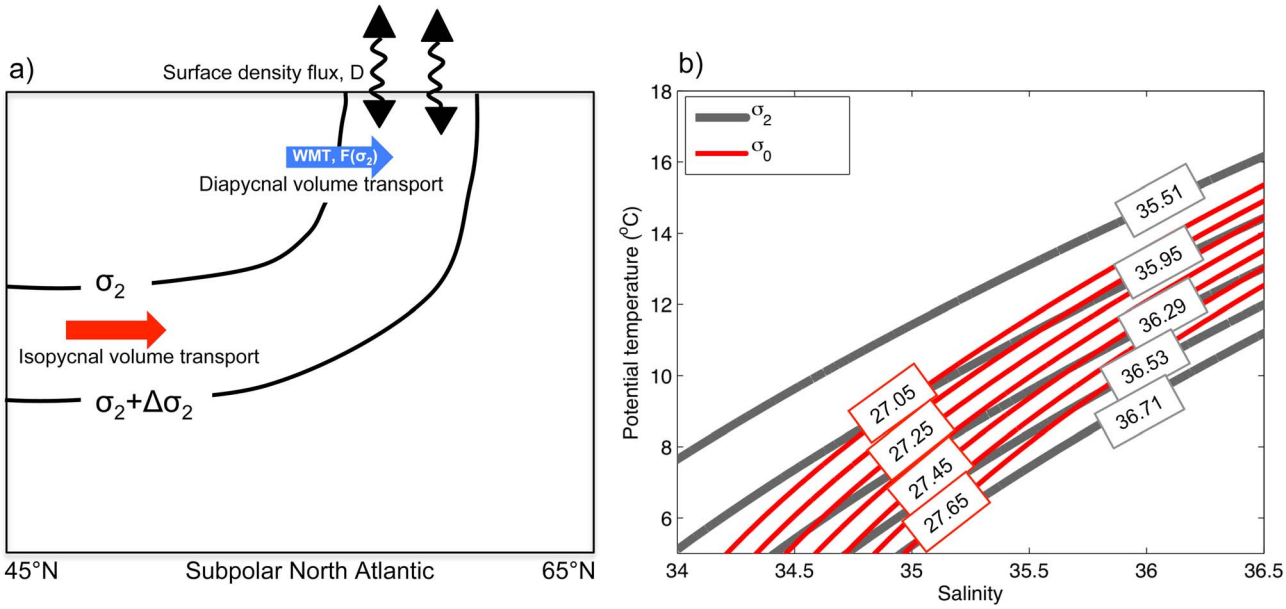

Figure 2. (a) Schematics to describe surface forced water mass transformation (WMT). WMT of surface water from one density class to another class due to surface density fluxes is equivalent to diapycnal volume transport (adapted from *Brambilla et al.* [2008]). (b) The typical density range of Subpolar Mode Water from observational studies is shown in red curves (in σ_0), and the density range used to capture the models' Subpolar Mode Water is illustrated by gray curves (in σ_2).

[22] In practice, to obtain geographical maps of the annual mean surface forced WMT across a given σ-isopycnal from monthly data we calculate for each grid cell the surface density flux between σ and $\sigma + \Delta\sigma$ and average over one year:

$$F_i(\sigma) = \frac{1}{N_T \Delta\sigma} \sum_{n=1}^{N_T} D_{n,i} \; dA_i \qquad (5)$$

where N_T is 12 (months in a year). Note that F from equation (4) is the integral over the whole outcrop region, whereas F_i from equation (5) is computed at each grid cell. The annual mean F_i is given in units of Sv (1 Sv = 10^6 m^3 s^{-1}).

[23] It has been found that WMT computed from monthly data, such as the observation-based estimate of *Brambilla et al.* [2008], tends to overestimate actual WMT. Eddies in the upper ocean and mixing associated with deepening of the mixed layer contribute in particular oppositely to surface forced WMT [*Tandon and Zhao*, 2004; *Cerovečki and Marshall*, 2008]. In this study we use climate models that are non-eddy resolving, and hence, the simulated surface forced WMT is possibly larger than the actual WMT (but also possibly more consistent with the applied diagnosis).

[24] Another practical aspect of calculating surface forced WMT is the identification of outcrop regions. The summer outcrop for a given density can be located far away from the winter outcrop for the same density. For instance, cold meltwater in the vicinity of the Arctic sea ice edge during summer could have similar densities as Subpolar Mode Water during winter. This means that when integrating the surface forced WMT over a year and a specific region, the water masses with the same density do not necessarily communicate with each other over a year.

[25] The surface forced WMT (F, see equation (5)) is dependent on the outcrop region that is determined by the density range ($\Delta\sigma$); the larger the range, the larger the outcrop area. This implies that F more represents the WMT in a σ-range given by a specific discretization, rather than a point estimate. The estimated transformation should nevertheless be independent of this to leading order; the area of the outcrop region is divided by the density range in (5). We have chosen to use the isopycnal discretization of BCM for convenience and consistency. The simulated surface forced WMT is therefore calculated for the interval 35.50 < = σ_2 < = 36.80 kg m^{-3}. These σ_2-densities are comparable with the observed density range of Subpolar Mode Water (Figure 2b) [*Brambilla and Talley*, 2008; *Brambilla et al.*, 2008]; $\Delta\sigma$ in equation (5) is the difference between the σ_2-densities for the simulated WMT (gray lines in Figure 2b).

[26] To evaluate the method of *Walin* [1982] for the present purpose, we compare the estimated surface forced *formation* and the explicit divergence of isopycnal transport in the subpolar region. The surface forced formation is the difference in surface forced WMT across two neighboring density layers. If there is convergence, water will subduct in the densest layer of the two, i.e., accumulation of water in the densest layer, and vice versa in case of divergence, i.e., removal of water in the densest layer. Hence, this surface forced formation expresses changes in the isopycnal transport (Figure 2a). If there is no difference in WMT across the two neighboring density layers, there is no formation of water masses (only transformation), and no change in the isopycnal transport. AMOCσ is the explicit isopycnal transport in the models. The surface forced formation in the subpolar region is therefore compared with changes in the isopycnal transport within the subpolar region obtained from the AMOCσ (this is done in section 4.3).

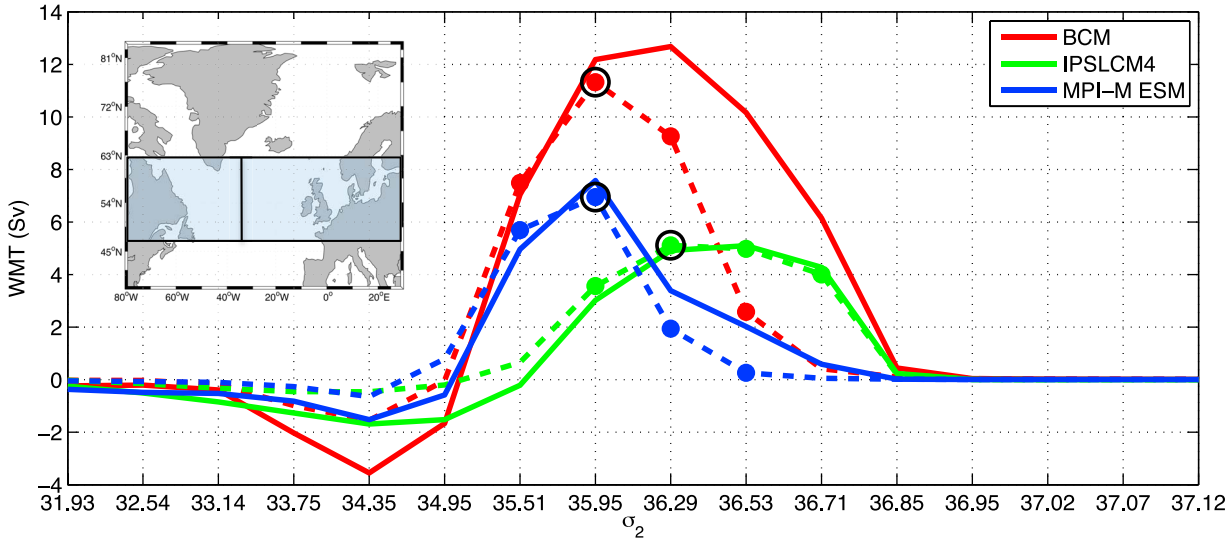

Figure 3. Annual mean surface forced water mass transformation (WMT) as a function of density, integrated over the entire subpolar region (48°N–62°N as indicated in the inset; solid lines) and over the eastern subpolar region (east of 35°W; dashed lines). The WMT has been estimated for each month, and the annual mean is then averaged over 500 years. Filled circles indicate the density range that corresponds to the WMT shown in Figures 5–7, whereas the black circle indicates the maximum WMT in the eastern subpolar region.

[27] A similar comparison was done by *Marsh* [2000], who integrated the total water mass formation north of 15°N and compared this with the diapycnal overturning circulation at that latitude. However, to do such a comparison, some assumptions have been made; interior mixing and volume changes of isopycnal layers are neglected. This means that the eventual expansion of a given layer due to surface forcing in this framework is interpreted as a convergence in the isopycnic flow at the boundaries of the region investigated. This should not be a considerable source of error for mean circulations, e.g., Figures 5–7, as a 0.1 Sv-imbalance would add a O(100 m) thick mean layer across the North Atlantic for a given density class during a multicentury simulation.

2.4. Statistical Methods

[28] To filter out high-frequency variability, all yearly time series have been low-pass filtered using an 11-year running Bartlett window. The time series are linearly detrended prior to correlation/regression and Empirical Orthogonal Function (EOF) analysis. For significance testing a Student's *t*-test is used together with the method of *Chelton* [1983] to estimate the effective number of degrees of freedom. All quantified correlations are significant at the 95% confidence level.

3. Surface Forced Water Mass Transformation

[29] In this section the simulated mean surface forced WMT is compared among the models and with observation-based WMT. Here we only highlight the differences and similarities, whereas in section 4 *reasons* for the differences are described. Before presenting the more detailed geographical distribution of WMT, the *integrated* WMT over the entire and eastern subpolar region are compared among the models.

[30] The integrated surface forced WMT demonstrates where the bulk of WMT occurs, and allows for quantitative comparison among the models. The integrated WMT over the entire subpolar region (48–62°N) and over the eastern region (east of 35°W) are shown as a function of density in Figure 3. The figure illustrates which model isopycnals outcrop in the subpolar region. For IPSLCM4 and MPI-M ESM, nearly all of the WMT occurs in the eastern part. This is also the case for BCM for $\sigma_2 \leq 35.95$ kg m^{-3}, but for higher densities the WMT occurs mainly in the western part. The WMT in the subpolar region is generally stronger in BCM than in the other two models. The WMT in IPSLCM4 occurs for slightly denser water masses than in MPI-M ESM.

[31] We use the same methodology as *Brambilla et al.* [2008] (cf. section 2.3); their observation-based surface forced WMT therefore provides a benchmark for assessing model performance in the subpolar region (Figure 4). The observation-based WMT is shown for the density range given in Figure 2b (σ_0 = 27.05–27.65 kg m^{-3}), where observation-based WMT predominantly is found [*Brambilla et al.*, 2008]. The geographical distribution of the simulated WMT is also shown in Figures 5–7 for the density range that corresponds to the largest simulated WMT (Figure 3) for each of the three models. The simulated WMT and the observation-based estimate are intercompared according to their geographical structure. The magnitude of WMT (i.e., for each grid cell) cannot be accurately compared, since the horizontal resolution of the models and the observation-based data differ. BCM nevertheless has the strongest WMT of the three models (Figure 3).

[32] The structure of surface forced WMT in BCM is in qualitative agreement with the observation-based estimate (Figure 5). More specifically, BCM has strong WMT just south of Nova Scotia and toward the eastern subpolar region. The position of the North Atlantic Current in BCM [*Langehaug et al.*, 2012] is less consistent with observation-based estimates (Figure 4) [see also *Krauss*, 1986; *Pérez-Brunius et al.*, 2004], thereby giving somewhat different regions of strong

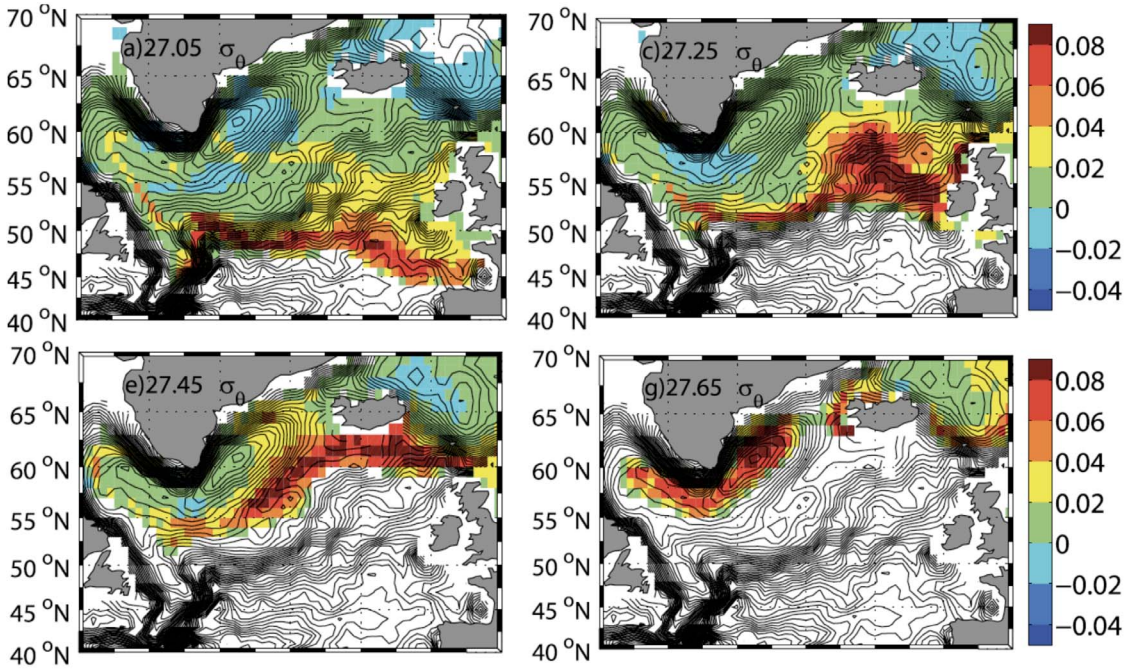

Figure 4. Observation-based annual mean surface forced water mass transformation (Sv) is shown in color. The corresponding density is noted in the figures. Positive values denote densification. Values are plotted on a regular 1° × 1° grid. The black lines are the surface flow streamlines [after *Brambilla et al.*, 2008].

WMT. For instance, in BCM there is strong WMT south of 45°N, which is not the case in the observation-based estimate. The models' North Atlantic Current is further described in the next section. The BCM is nevertheless more similar to the observation-based WMT in this aspect than the other two models. Model outcrop regions in March are indicated in Figures 5–7. Even though our computation of WMT follows the outcrop positions in their seasonal movement, we show March outcrops that are typical of the most active season for WMT.

[33] The IPSLCM4 surface forced WMT structure differs both from the observation-based and that of BCM (Figure 6). IPSLCM4 has strong WMT just south of Nova Scotia, but between this region and the eastern subpolar region the WMT is weak (less than 0.01 Sv). The structure of the WMT in IPSLCM4 is more similar to BCM and the observation-based WMT in the vicinity of the Greenland-Scotland Ridge.

[34] The MPI-M ESM displays a different surface forced WMT structure than both the other two models and the observation-based estimate (Figure 7). Here WMT mainly occurs along the eastern boundary of the North Atlantic Basin and the Nordic Seas. Similar to IPSLCM4, MPI-M ESM has strong WMT just south of Nova Scotia and weak WMT between Nova Scotia and the eastern subpolar region. The WMT for the lowest densities are negative east of Newfoundland (Figures 7a and 7b), meaning that the surface water becomes less dense here. Negative WMT close to Newfoundland is also seen in BCM and IPSLCM4, although not so extensively.

[35] To emphasize the relevance of the identified model differences, we show the simulated zonal mean heat flux and poleward heat transport in the northern North Atlantic Ocean (Figure 8). The poleward heat transport is strongly interconnected with the surface heat flux, and hence, also the surface forced WMT. For instance, in regions with large heat convergence, there is consistently large heat loss from the ocean to the atmosphere. The meridional distribution of the ocean heat transport is thus a quantification of the ocean's influence on climate, identifying where and how much heat is lost from the ocean to the atmosphere (or stored in the ocean). The largest heat loss occurs just south of Nova Scotia and close to the Greenland-Scotland Ridge in all models, and between 43°–50°N there is warming of the ocean surface in IPSLCM4.

[36] The simulated poleward heat transport is shown together with estimates from reanalysis data in Figure 8 (bottom). It is important to note again that the reanalysis data contain large uncertainties [e.g., *Rhines et al.*, 2008]. Nevertheless, the ECMWF and NCEP derived heat transports compare relatively well in the northern North Atlantic. BCM is the most similar to the reanalysis data at the border between the subtropical and subpolar region, whereas the two other models are more similar to the reanalysis data in the northern part of the subpolar region, close to the Greenland-Scotland Ridge.

[37] We have seen that there are large differences in how the three models simulate their surface forced WMT, both in terms of geographical distribution and the magnitude of integrated WMT over the subpolar region. The comparison of northward ocean heat transports also highlight differences in the location and strength of surface heat loss.

4. Identifying Causalities in Model WMT

[38] The model differences in WMT, including their comparison with observation-based and reanalysis data, are here diagnosed based on model heat and freshwater fluxes.

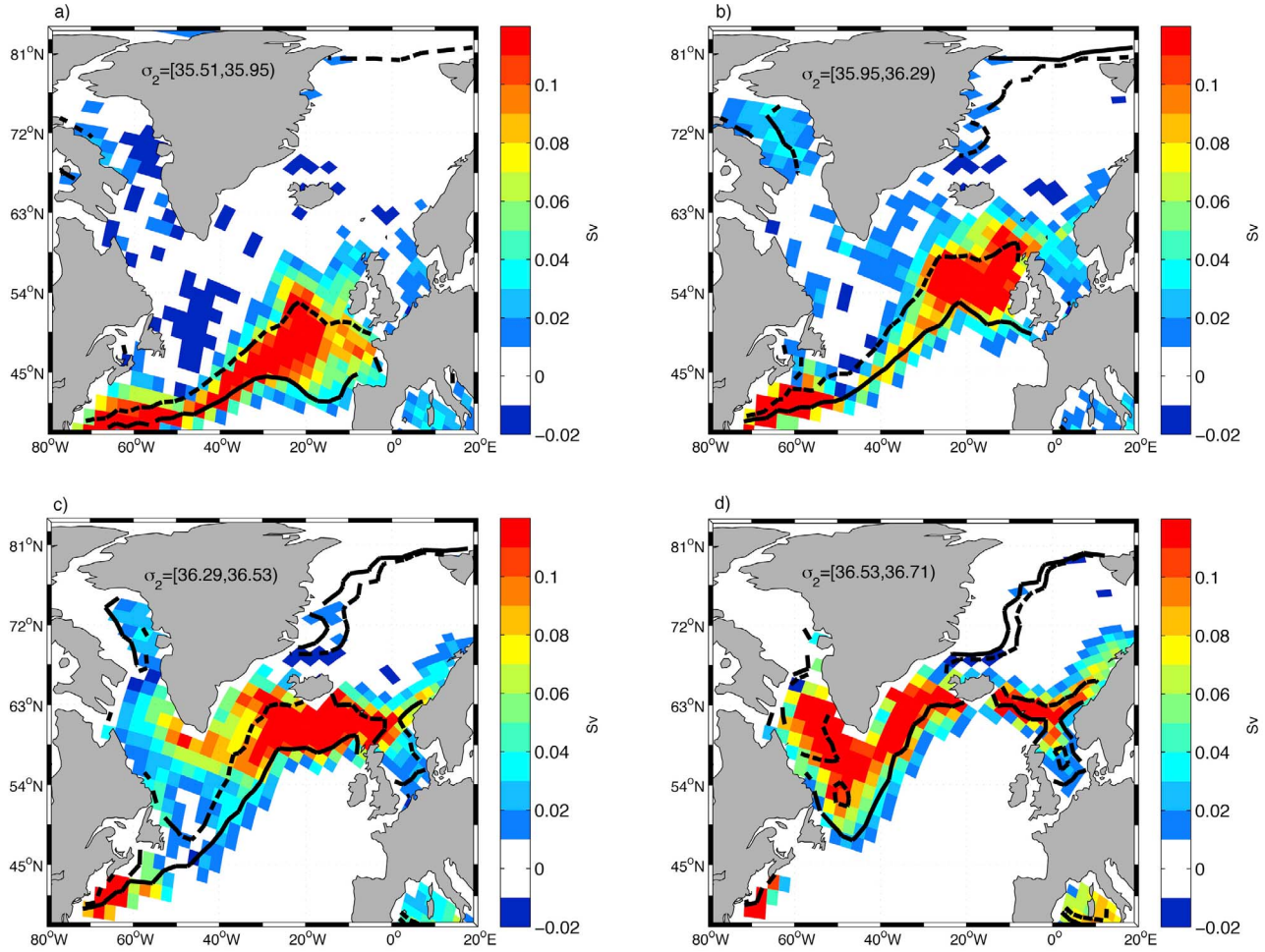

Figure 5. BCM's annual mean surface forced water mass transformation (WMT) is shown in color. The WMT has been estimated for each month, and the annual mean is then averaged over 500 years. Positive values denote densification. The corresponding σ_2-density range is noted in the figures. The upper and lower boundary of this range in March is indicated by dashed and solid lines, respectively.

4.1. Heat and Freshwater Fluxes

[39] Two main differences stand out when comparing heat and freshwater fluxes. The first is associated with the large heat loss along the pathway of the North Atlantic Current and in the Labrador Sea (Figure 9, left). The observation-based pattern is relatively well reproduced in BCM, except that the pathway of the North Atlantic Current is shifted eastward compared the observed (as identified in section 3). In contrast, the two other models have little heat loss between Nova Scotia and the eastern subpolar region. The reason for the weak heat loss in IPSLCM4 is that the North Atlantic Current subducts beneath what has been found to be a much too fresh surface layer in this region [*Mignot and Frankignoul*, 2010], leading to weak WMT. The second difference is the excessive freshwater input close to Newfoundland in IPSLCM4 and MPI-M ESM compared to NCEP and BCM (Figure 9, right). This excessive freshwater input can be explained by excessive net precipitation regionally in these models compared to NCEP, which in the case of IPSLCM4 has previously been described by *Swingedouw et al.* [2007].

[40] The heat and freshwater fluxes' relative contribution to the total density flux are compared in Figure 10. The density flux determines the magnitude of the WMT (equations (1) and (4)). The thermal contribution is mainly positive (i.e., density gain from heat loss (Figure 10, left)), whereas the haline contribution is mainly negative (i.e., density loss from freshwater input (Figure 10, right)). The thermal contribution dominates the density flux in the eastern subpolar region (cf. Table 1) and in the Atlantic domain of the Nordic Seas (Figure 1a). Generally, the thermal contribution in BCM is larger than that in IPSLCM4 and MPI-M ESM (Table 1). The haline contribution dominates or is comparable to the thermal contribution in the Polar/Arctic domain of the Nordic Seas (Figure 1a). In the western subpolar region the three model simulations generally differ: The thermal contribution dominates in BCM, whereas, consistent with an apparent overestimate of freshwater input (Figure 9), the haline contribution dominates in IPSLCM4 and is comparable to the thermal contribution in MPI-M ESM (Table 1).

[41] Overall, the northward flowing water becomes denser due to the predominantly positive WMT (Figure 5–7),

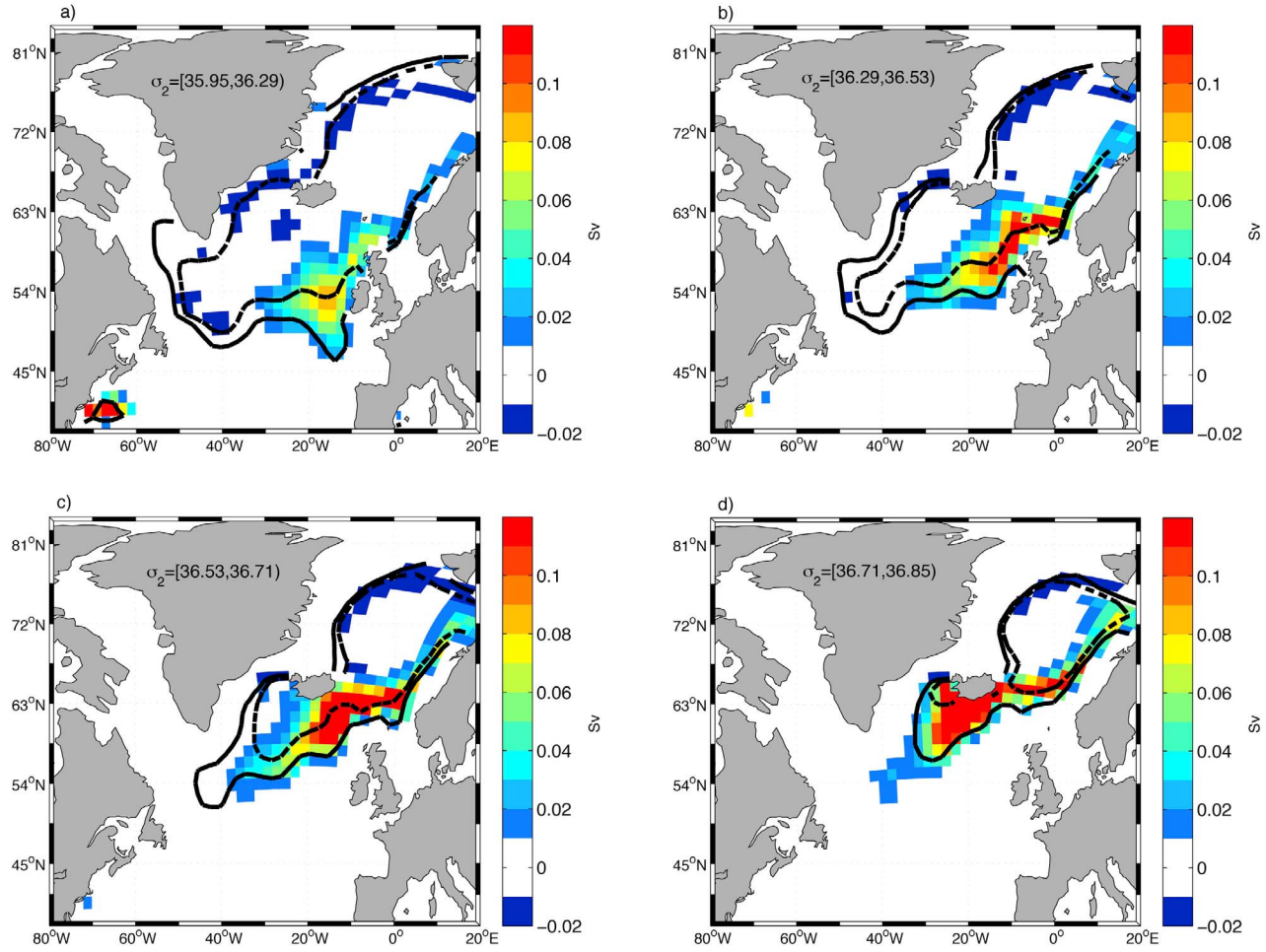

Figure 6. IPSLCM4's annual mean surface forced water mass transformation (WMT) is shown in color. The WMT has been estimated for each month, and the annual mean is then averaged over 500 years. Positive values denote densification. The corresponding σ_2-density range is noted in the figures. The upper and lower boundary of this range in March is indicated by dashed and solid lines, respectively.

caused by a dominance of heat loss over freshwater input. In IPSLCM4 the *integrated* thermal contribution in both the subpolar region and the Nordic Seas is only slightly larger than the integrated haline contribution (Table 1). However, there is positive WMT *regionally*, such as in the eastern subpolar region (Figure 3). A general dominance of the thermal over the haline buoyancy forcing in the subpolar region is also found in both high- and coarse resolution ocean models forced with reanalysis data [*Gulev et al.*, 2007].

[42] In order better to understand the differences in the haline component of the models, the models' Arctic sea ice extent is included in Figure 10 (right). The freshwater input in the Nordic Seas in BCM and IPSLCM4 is located close to the extremes in September sea ice extent throughout the simulations, suggesting that this freshwater input is dominated by sea ice melting. Similar freshwater input in the Nordic Seas is not evident in MPI-M ESM. This can thus be related to the absence of sea ice melting/freezing in the diagnosed freshwater budget of MPI-M ESM. Both in IPSLCM4 and MPI-M ESM the sea ice extent in March advance farther south than observed in present climate [*Arzel et al.*, 2006], whereas BCM is more similar to what is observed. This means that winter sea ice cover in IPSLCM4 and MPI-M ESM largely prevents heat loss in the Labrador Sea, and hence reduces regional deep water formation.

[43] To estimate the magnitude of temporal variations, the standard deviation (std) of interannual variability of the thermal and haline component is calculated (Figure 10, black contours; using non-filtered time series). In BCM and IPSLCM4 the haline contribution has largest variability in the Irminger Sea/Denmark Strait and the Polar/Arctic domain of the Nordic Seas. In the same regions, the haline contribution has low variability in MPI-M ESM, which again can be related to the lack of sea ice melting/freezing in the diagnosed freshwater budget of this model. The thermal contribution has largest variability along the pathway of the models' North Atlantic Current, which is shown in following section. In BCM there is also large variability in the Labrador Sea, whereas variability is low in the other two models in this region. In BCM the thermal variability in the Atlantic domain of the Nordic Seas is of similar magnitude to the variable heat loss associated with the North Atlantic Current. This is also the case for MPI-M ESM, but not for IPSLCM4.

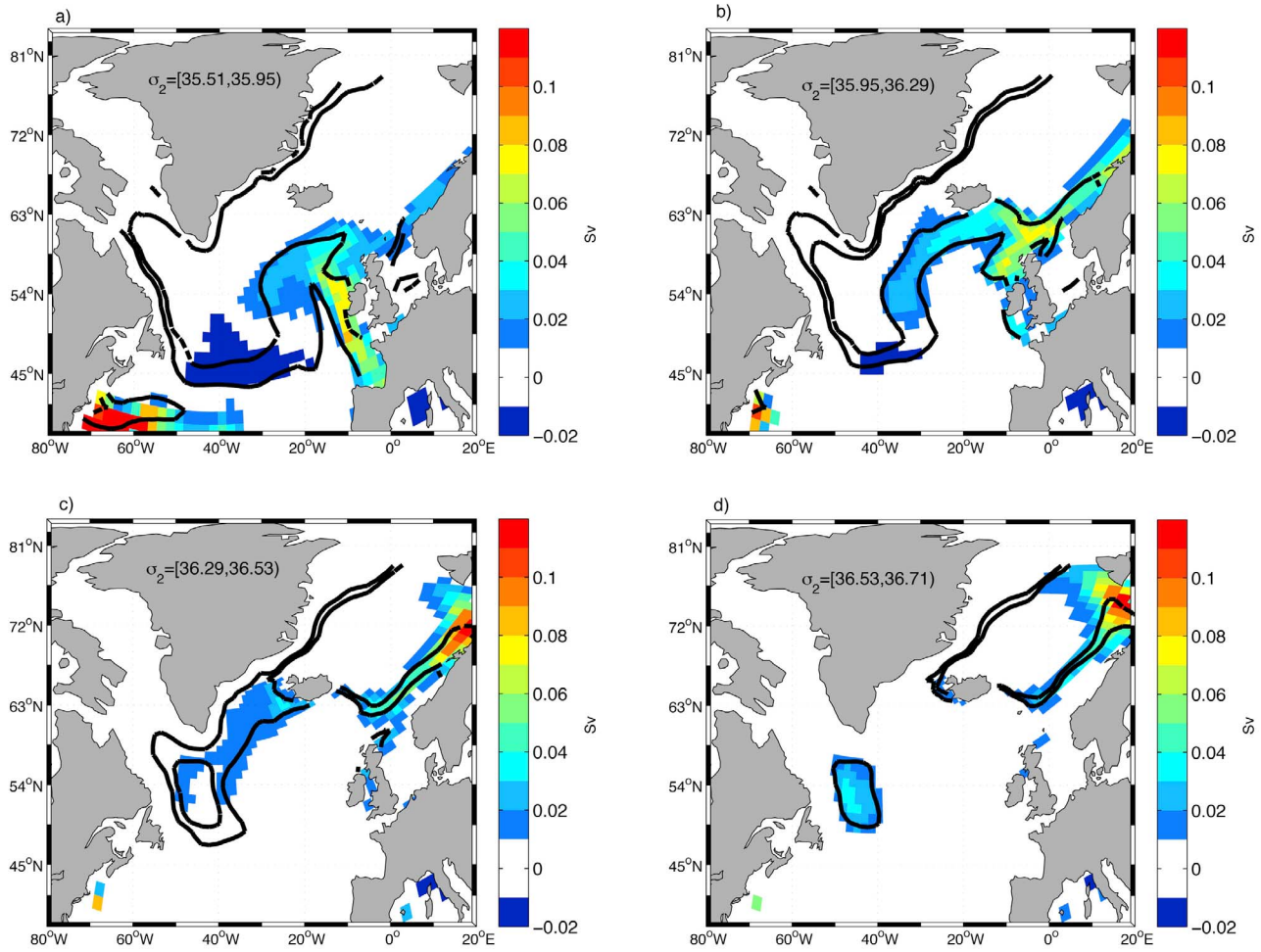

Figure 7. MPI-M ESM's annual mean surface forced water mass transformation (WMT) is shown in color. The WMT has been estimated for each month, and the annual mean is then averaged over 500 years. Positive values denote densification. The corresponding σ_2-density range is noted in the figures. The upper and lower boundary of this range in March is indicated by dashed and solid lines, respectively.

4.2. The North Atlantic Current

[44] The border between the Subpolar and Subtropical gyres outlines the pathway of the North Atlantic Current. The models' Subpolar and Subtropical gyres are manifested in the barotropic stream function with cyclonic (negative) and anticyclonic (positive) circulations, respectively (Figure 11). The North Atlantic Current is observed to curve around Newfoundland before it turns northeastward in the "Northwest Corner" [e.g., *Arhan*, 1990; *Krauss*, 1986; *Pérez-Brunius et al.*, 2004], but splits from the coast too far south in all three models. In MPI-M ESM the North Atlantic Current has a zonal direction, crossing the North Atlantic basin before flowing northward along its eastern rim. This is consistent with this model's weak WMT between Nova Scotia and the eastern subpolar region, and strong WMT along the eastern rim of the basin. In BCM and IPSLCM4 the North Atlantic Current separating the two gyres has a similar northeastward pathway, but the strength of the circulation is weaker in the latter. In addition, as mentioned before, the North Atlantic Current subducts beneath a fresh surface layer in this model. The North Atlantic Current is in reality a very complex, eddy-rich junction between the two gyres [*Hecht and Smith*, 2008]. The three models represent it very differently from one another and from the eddy rich observed state. Thus is seems crucial to investigate the structure of the North Atlantic Current in the models.

[45] The above differences are also manifested in surface density structure (Figure 11). The North Atlantic Current is characterized by a strong surface density gradient in the surface density. This front between subpolar and subtropical waters is clearly seen in BCM and MPI-M ESM, although in different locations, but not in IPSLCM4 due to the fresh surface layer capping the North Atlantic Current. Both IPSLCM4 and MPI-M ESM have less dense surface water in the westernmost subpolar region than BCM, consistent with the large freshwater input in this region in IPSLCM4 and MPI-M ESM. However, in all models there is a gradual densification of the surface water flowing with the North Atlantic Current in the eastern subpolar region, and also for the continuation of the flow in the Nordic Seas.

[46] The gradual densification of surface water carried by the North Atlantic Current is also illustrated in Figure 12 (left) (see incline of isolines in the dashed rectangles). This figure

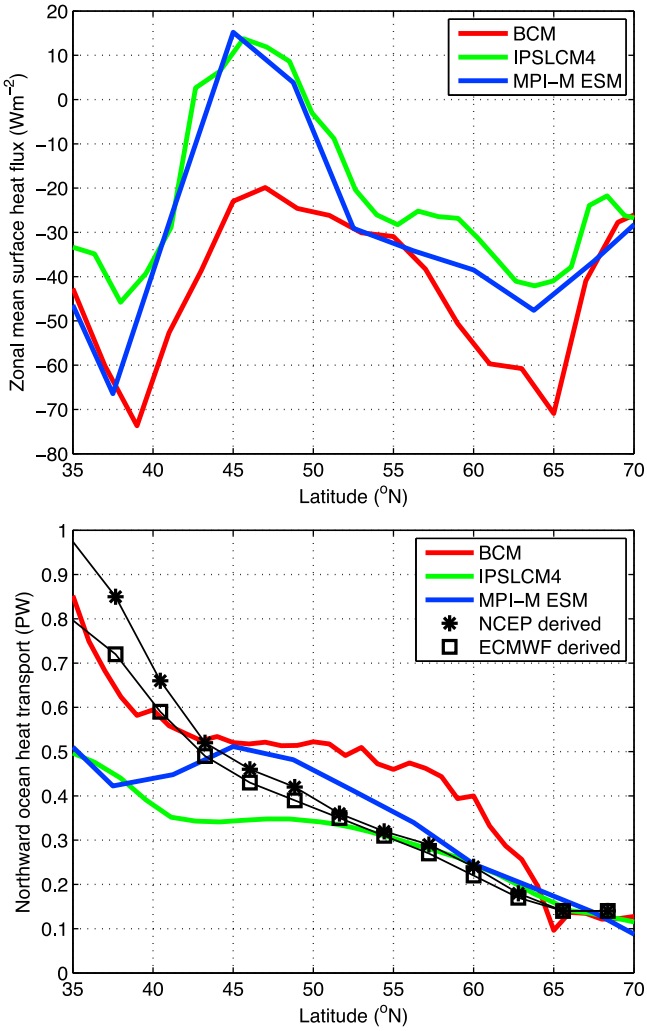

Figure 8. (top) Zonal mean surface heat flux and (bottom) northward ocean heat transport in the subpolar North Atlantic over 500 years for the three models. The black squares and asterisks denote the ocean heat transport based upon surface fluxes for 1985 to 1989 for NCEP and ECMWF reanalysis products [*Trenberth and Caron*, 2001].

shows the density distribution associated with the zonally integrated ocean circulation, i.e., AMOCσ. The densification is consistent with the overall positive surface forced WMT in the subpolar region and the Nordic Seas. The densification is the strongest in BCM. The weak surface forced WMT between Nova Scotia and the eastern subpolar region (43–48°N) in IPSLCM4 and MPI-M ESM compared to BCM is also manifested in the models' AMOCσ (Figure 12).

[47] The AMOCσ captures the densification associated with the Subpolar Gyre (Figure 12, between 45 and 60°N for the entire density range). The essentially horizontal gyre circulation has, on the other hand, little imprint on AMOCz (Figure 12, right). This implies a stronger AMOCσ than AMOCz in the subpolar region, and in general, an overturning circulation cell that extends farther north. The BCM and MPI-M ESM have comparable maximum value of the AMOCz between 20 and 60°N (18.6 Sv and 16.4 Sv, respectively, at 31.5°N), while the maximum value for IPSLCM4 is about half (9.6 Sv at 44°N). The maximum value of the subpolar AMOCσ – as for AMOCz – is much lower for IPSLCM4 (9.4 Sv at 53°N) than in the two other models (18.3 Sv at 58°N and 51°N for BCM and MPI-M ESM, respectively). Hence, the ranking of the models is similar regarding the maximum value of both AMOCσ and AMOCz, although the maxima are shifted toward the subpolar region in AMOCσ. The latter is consistent with the observations of *Talley et al.* [2003].

[48] The structure and strength of AMOCz in BCM and MPI-M ESM are comparable even though the surface forced WMT is quite different between the two. This demonstrates the importance of applying analyses complementary to the frequently used AMOCz. We accordingly promote the analysis exemplified herein – the estimation of surface forced WMT and its geographical distribution.

4.3. Evaluation of the Estimated Surface Forced Water Mass Transformation

[49] AMOCσ quantifies zonally integrated WMT directly from the actual isopycnal transports, whereas the approach of *Walin* [1982] *estimates* the WMT from surface density fluxes. To investigate how the latter represents actual WMT in the models, we compare the estimated surface forced formation (cf. section 2.3) and isopycnal transports obtained from AMOCσ (Figure 12, left). The surface forced formation is calculated for all isopycnals that outcrop in the region 48°–62°N. The surface forced formation has a similar structure in all models, i.e., removal of water masses with lighter densities and subduction of water masses with denser densities (Figure 13). The difference in the isopycnal transport between the northern (62°N) and southern (48°N) boundary of the subpolar region corresponds well with the estimated surface forced formation in IPSLCM4 and MPI-M ESM, but less well for BCM (Figure 13).

[50] One reason for the difference between the surface forced formation and net isopycnal transport through the subpolar region in BCM is the model parameterization of deep convection, as described in section 2.1. Due to the instantaneous re-stratification at each time step in the model simulation, there is no outcropping associated with this process in our diagnosis; parts of the water attributed to BCM's isopycnal layers $\sigma_2 = 36.53$ kg m^{-3} and $\sigma_2 = 36.71$ kg m^{-3} (red curve in Figure 13) are placed in the model's denser layers by deep convection (black curve in Figure 13).

[51] A perfect match between the surface forced formation and the net isopycnal transport through the subpolar region is not expected. The neglected diapycnal mixing is present to an extent in all models. For instance, the surface forced formation in MPI-M ESM cannot explain the positive isopycnal flow with density $\sigma_2 = 36.71$ kg m^{-3} (black curve in Figure 13). In BCM, the separate mixed layer makes the dynamics of the upper ocean in BCM different from the other two models. In particular, ad hoc vertical mixing is implicit to the mixed-layer model formulation as the layer is vertically homogenous by definition [*Eldevik*, 2002]. The magnitude of estimated surface forced formation is larger than the net isopycnal transport in the lighter layers of BCM through the subpolar region (Figure 13). This indicates that the implicit mixing acts to

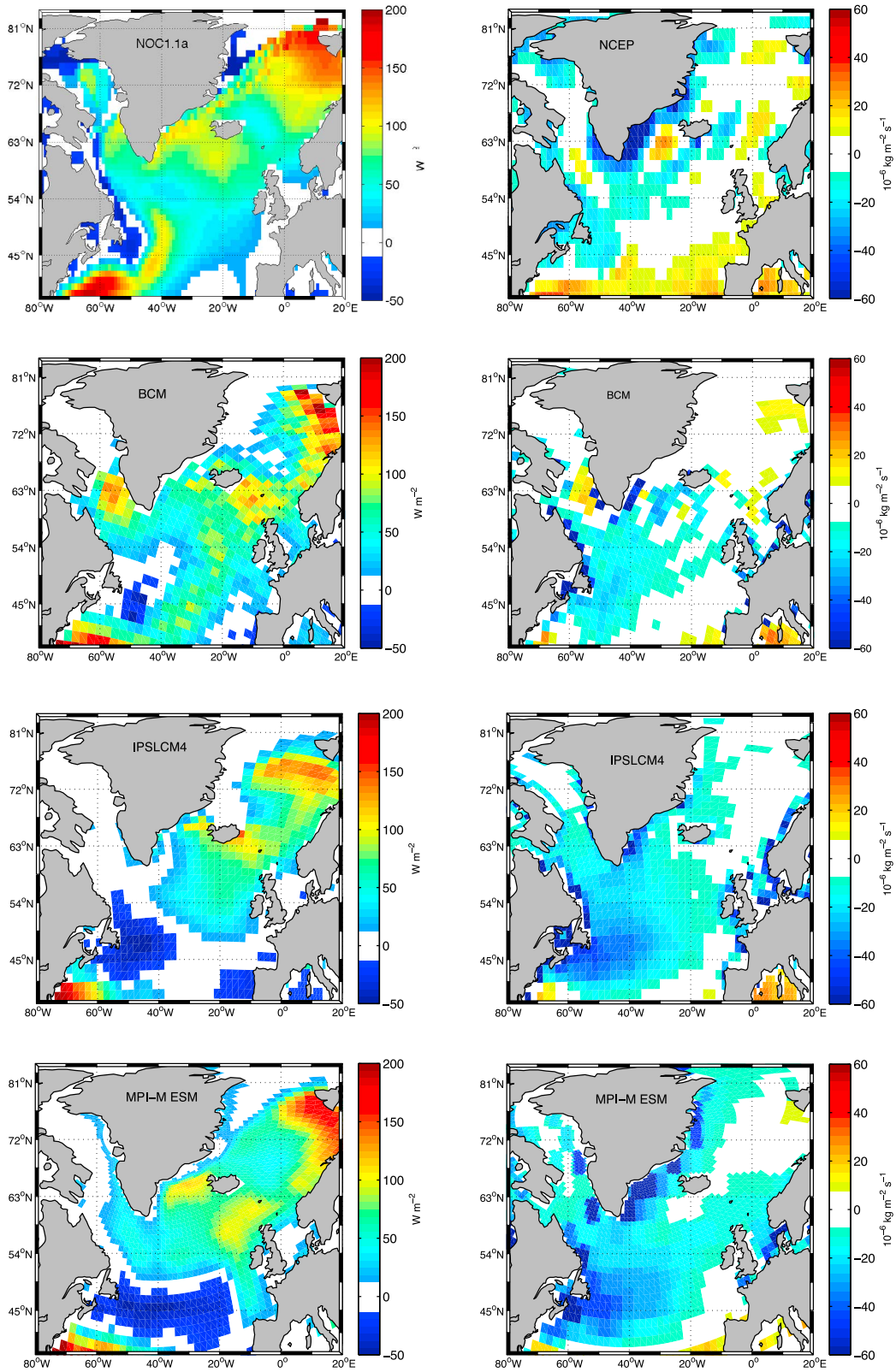

Figure 9. (left) Mean net heat loss from ocean (W m^{-2}) and (right) net freshwater loss from ocean (quantified as virtual salt flux, kg m^{-2} s^{-1}) over 500 years for the three models. The observation-based and reanalysis data (first panel) are averaged over the period 1980–1993 and 1948–2010, respectively. The freshwater flux is calculated from: Precipitation - Evaporation + Runoff. Model names and source for observation-based and reanalysis data are indicated in the upper left corner of the figures.

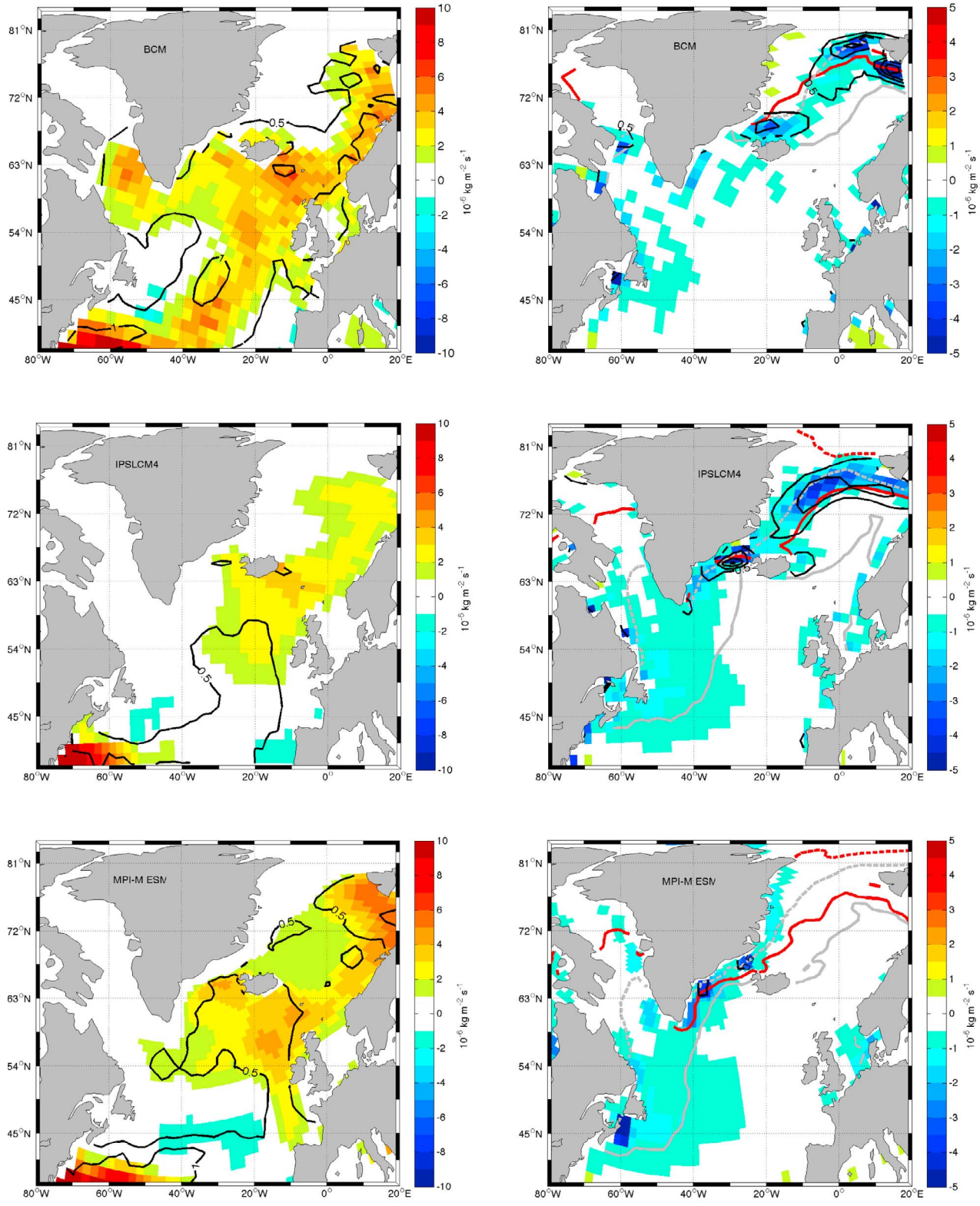

Figure 10. (left) Mean thermal (F_T) and (right) haline (F_S) contribution to the density flux into the ocean over 500 years for the three models, given in 10^{-6} kg m^{-2} s^{-1}. Positive values indicate densification. Model names are indicated in the upper left corner of the figures. Note the different scales on the color bars between F_T and F_S, and that ice melting/freezing is not taken into account in the F_S for MPI-M ESM. One standard deviation of the interannual variability of F_T and F_S are shown by black contours with intervals of 0.5. The red solid (dashed) lines indicate maximum (minimum) sea ice extent in September. The lines are drawn where the sea ice percentage is zero. Likewise for the gray lines, but for March.

Table 1. Mean Thermal (F_T) and Haline (F_S) Contribution to the Surface Density Flux[a]

	BCM		IPSLCM4		MPI-M ESM	
Region	F_T	F_S	F_T	F_S	F_T	F_S
E subpolar	2.72	−0.35	1.25	−0.47	2.22	−0.41
W subpolar	1.18	−0.55	−0.02	−1.00	0.72	−0.77
subpolar	2.14	−0.44	0.78	−0.66	1.49	−0.57
Nordic Seas	2.20	−0.59	1.13	−1.07	1.50	−0.86

[a] F_T and F_S (in 10^{-6} kg m^{-2} s^{-1}) is calculated for the Nordic Seas (63–79°N, 40°W–20°E) and the eastern (E) and western (W) subpolar region (47–63°N, 60°W–10°E). The regions for each model are found by including the grid cells that are located within the longitude and latitude limits. Since the models grids are not similar, the regions will be slightly different among the models. The eastern and western region is separated at 35°W. Note that sea ice melting/freezing is not taken into account in the F_S for MPI-M ESM.

reduce the effect of the surface forced WMT, consistent with the findings of *Nurser et al.* [1999].

[52] In summary, the method introduced by *Walin* [1982] provides a simple and useful way of estimating surface forced WMT in climate models, and it compares relatively well with the models' actual subpolar WMT as described by diapycnal overturning in AMOCσ.

5. Decadal Variability

[53] Several model studies have shown that decadal climate variations are linked to variations of AMOC [e.g., *Eden and Willebrand*, 2001; *Bentsen et al.*, 2004; *Deshayes and Frankignoul*, 2008; *Kwon and Frankignoul*, 2011]. At longer timescales, Atlantic Multidecadal Variability (AMV) is seen, for example with two major and several minor warm periods in the subpolar region during the 20th Century [e.g., *Enfield et al.*, 2001]. In fact the early 20th Century warming (1930s–1960s) is one of the largest naturally occurring climate events in the instrumental record and the post-1995 event expresses the current warm period. AMV has been associated with clustered atmospheric blocking patterns over the northern Atlantic and with changes in the warm branch of the AMOC [*Häkkinen et al.*, 2011a, 2011b].

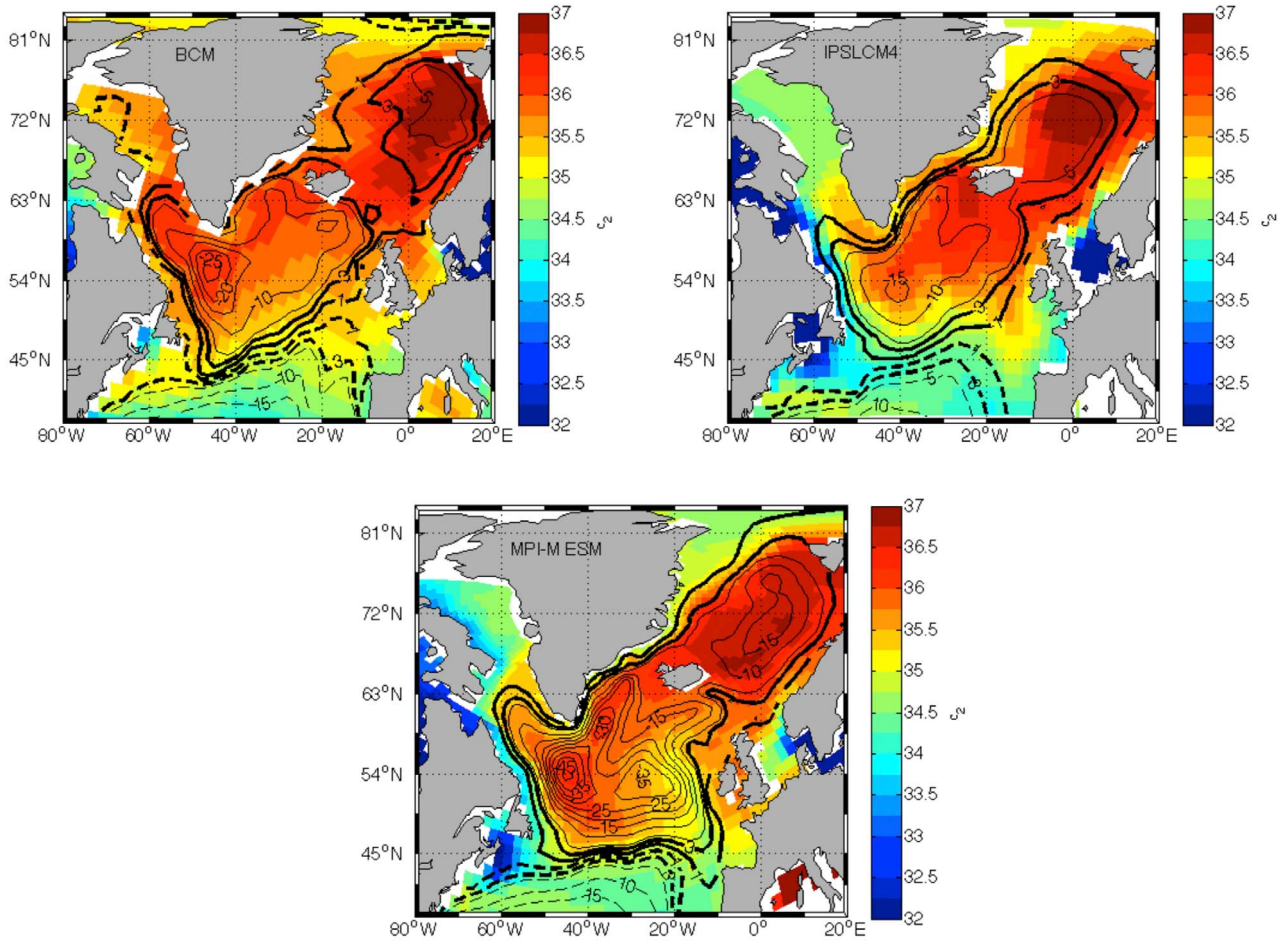

Figure 11. Mean surface density (in σ_2) over 500 years for the three models. Model names are indicated in the upper left corner of the figures. Mean barotropic stream function over 500 years is shown in black contours (numbers are given in Sv), where negative (positive) stream function indicates the Subpolar (Subtropical) Gyre. Thin contours are shown with intervals of 5 Sv. Thick contours are shown for ±1 Sv and ±3 Sv, to emphasize the position of the North Atlantic Current at the border between the Subpolar and Subtropical gyres.

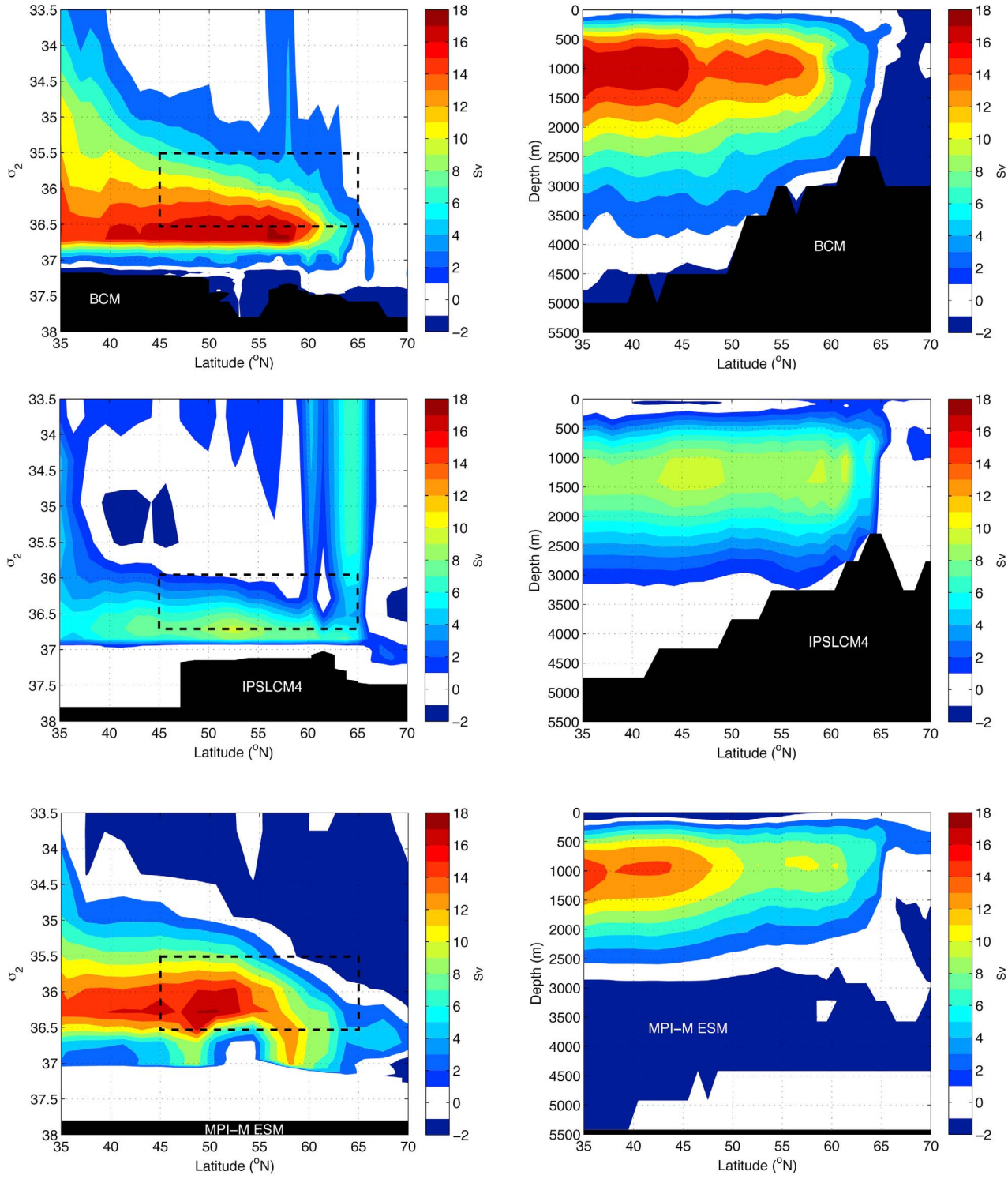

Figure 12. (left) Mean meridional overturning stream function in latitude-density space (AMOCσ) and (right) latitude-depth space (AMOCz) over 500 years for the three models. The density bins chosen for the computation of AMOCσ in IPSLCM4 and MPI-M ESM are consistent with the isopycnal discretization of the ocean model in BCM. Model names are indicated in the figures. The dashed rectangles illustrate the density range associated with the surface forced WMT shown in Figures 5–7. Note that the annual mean overturning circulation is used here, whereas the surface forced WMT is calculated from monthly values.

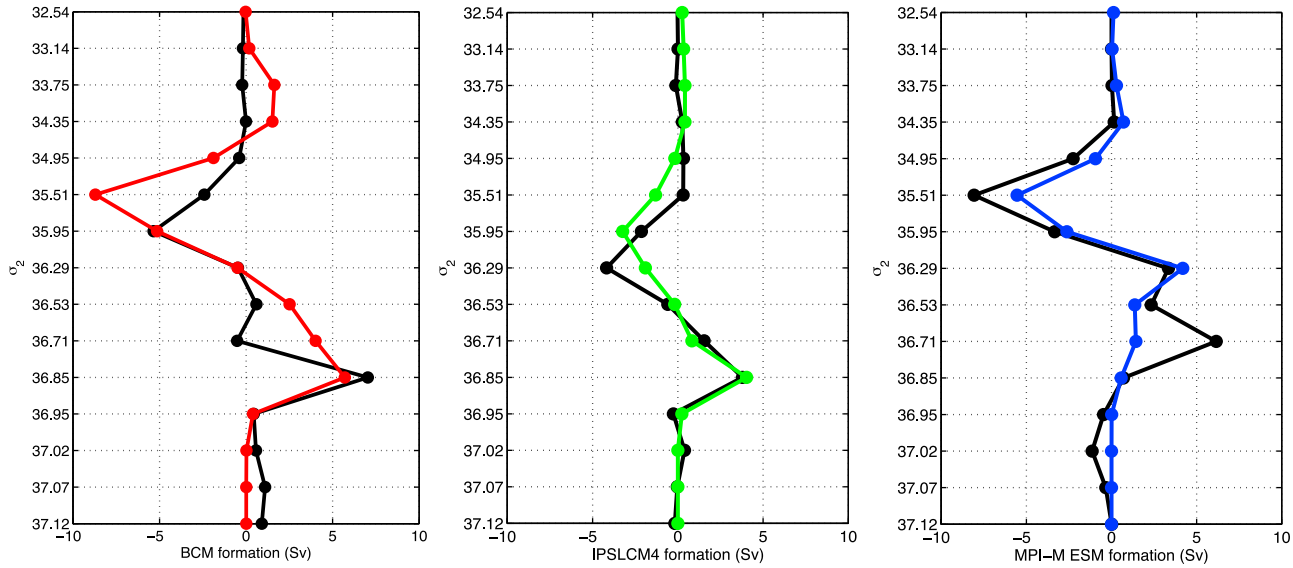

Figure 13. Annual mean surface forced water mass *formation* (i.e., divergence of the *transformation*) integrated over the subpolar region (colored lines; derivatives with respect to density of the solid curves in Figure 3). The region is indicated in the inset in Figure 3. The water mass formation has been estimated for each month, and the annual mean is then averaged over 500 years. The black lines show the models' divergence in the isopycnal transport by density bin, which is found by subtracting the transport profile in density bins at 48°N from the transport profile in density bins at 62°N.

[54] In this section, we investigate the variability of surface forced WMT and its link to the variable AMOCσ on decadal timescales. To represent the temporal evolution of WMT associated with Subpolar Mode Water, we use time series of maximum WMT in the eastern subpolar region (WMT_{max}; Figure 14). The variance of WMT_{max} in MPI-M ESM (std 1.8 Sv) is about three times larger than in BCM and IPSLCM4 (0.5–0.6 Sv). The larger variance in MPI-M ESM is also illustrated by a power spectrum of WMT_{max} (Figure 15). These spectra show that the power in MPI-M ESM resembles almost a red noise spectrum with higher energy at lower frequencies. This is not the case in the two other models, and it is actually the opposite in BCM with higher energy at higher frequencies. Both BCM and IPSLCM4 show most energy at seven yrs periodicity (arrow in Figure 15). MPI-M ESM has enhanced energy at 7, 13, 21, and around 50 yrs periodicity. Although the peaks are not significantly different from red noise, we here want to emphasize the enhanced variability on decadal timescales.

[55] To represent the variable AMOCσ, the first principal component from EOF analysis is used. The power spectra of the principal component for all three models almost resemble a white noise spectrum with comparable energy at all frequencies (not shown). In BCM and MPI-M ESM, there is slight increase of energy around 50 yrs periodicity. The first EOF of yearly AMOCσ is shown for the latitudinal band from 35°N to 70°N in Figure 16 (left), identifying the structure of most variance in AMOCσ. In BCM and MPI-M ESM the dominant pattern is a change in the southward flow in the dense layers and a weaker change of the opposite sign in lighter layers. Unlike AMOCz, variability of AMOCσ can also be related to expanding or shrinking of isopycnal layers; if the thickness of denser layers increases in a water column, the thickness of lighter layers in the same water column decreases accordingly (for instance as a result of deep convection). This change does not necessarily imply more southward volume flow over the water column, and hence, an immediate compensating change in the northward flow aloft is not required. This is in contrast to AMOCz, where a change in the southward deep flow must be compensated by a change in the northward flow aloft due to continuity. The lagged correlations demonstrate that an increase in the southward

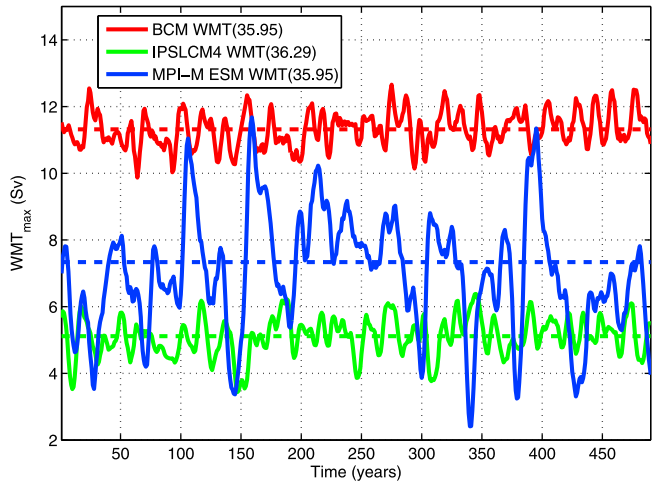

Figure 14. Time series of maximum surface forced water mass transformation in the eastern subpolar region (WMT_{max}). The WMT_{max} and the corresponding σ_2-density (indicated in the legend) for each model were found in Figure 3. The time series are filtered using an 11-year low-pass filter. The dashed lines illustrate the mean WMT_{max} for each model.

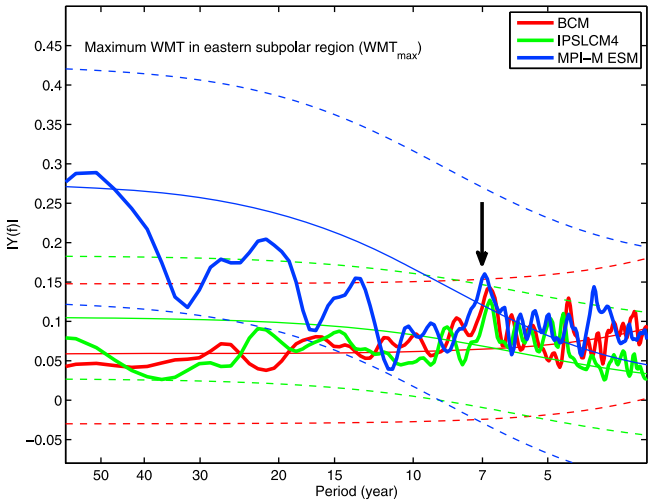

Figure 15. Power spectrum of the linearly detrended annual WMT data (thick line) together with the theoretical red noise spectrum (thin solid line) computed by fitting a first order autoregressive process with a 95% confidence interval (dashed lines) around the red noise. The spectrum is smoothed by a binomial filter with window length of nine years. The arrow indicates the enhanced energy at seven years periodicity.

dense flow (i.e., strengthening of EOF1 of AMOCσ) is not necessarily related to an immediate response in the northward flow, but leads an increase in the northward flow at 48°N by one year (Table 3 and magenta curves in Figure 16). The strength of the northward flow at both 48°N and 60–64°N is given in Table 2.

[56] A similar relationship was also found by *Grist et al.* [2009], with a lagged increase in the northward flow at 48°N after an increase in northern dense water formation. The latter includes the total formation north of 48°N, and hence, includes the formation of the densest water masses in the Nordic Seas and Labrador and Irminger seas. It is likely related to the variability of the dense southward flow, and therefore corresponds to our dominant mode of AMOCσ (Figure 16, left). In IPSLCM4 the dominant mode shows a simultaneous change in the entire AMOCσ, and hence, the northward flow at 48°N increases at zero time lag (Table 3 and Figure 16).

[57] To investigate the decadal relationship between WMT associated with Subpolar Mode Water and AMOCσ, WMT_{max} has been correlated with the first principal component of AMOCσ. The two are significantly correlated in BCM and MPI-M ESM, where WMT_{max} is found to *lag* AMOCσ (Table 3 and gray curves in Figure 16). This means that 7 to 8 years after an increase in the southward flow of dense water masses in the North Atlantic Basin there is an increase in the WMT, and hence, the heat loss in the eastern subpolar region. *Gastineau and Frankignoul* [2011] used the same model simulations as presented in this study, among others, and found that an intensification of AMOCz was followed by low sea level pressure anomalies over the North Atlantic, with a time lag of up to 10 years. They found that this atmospheric response was caused by increased northward oceanic heat transport, resulting in increased heat release along the pathway of the North Atlantic Current. We have seen from the lagged correlations above (Figure 16) that a strengthening of the dominant mode of AMOCσ is associated with an increase in the northward flow into the subpolar region. Hence, both this study and *Gastineau and Frankignoul* [2011] point to the variable northward flow as a source for the variable WMT (or heat loss) in the eastern subpolar region on decadal time scales, and that the variable WMT in this region is not a source of AMOC variability.

[58] Several recent studies assess decadal variability in temperature and salinity in the eastern subpolar region [e.g., *Johnson and Gruber*, 2007; *Thierry et al.*, 2008; *Häkkinen et al.*, 2011a]. The mechanisms suggested by these authors are different, or at least only implicitly related to the above, which relates WMT to the overturning circulation. *Häkkinen et al.* [2011a] suggest that wind-induced changes in the Subtropical and Subpolar gyres are responsible for observed thermohaline anomalies. For instance, the observed recent relaxation of the gyres' circulation leads to a contraction of the Subpolar Gyre and an expansion of the Subtropical Gyre. This change in the surface circulation forms a gateway for warm and saline anomalies to propagate from the Subtropical region to the Subpolar region [see *Häkkinen et al.*, 2011a, Figure 14]. However, the wind-driven horizontal gyres and the overturning circulation are highly interconnected. It is therefore not straightforward to identify the relationship between the overturning circulation and temperature anomalies in the northern North Atlantic. This is demonstrated in an intercomparison of all climate model simulations from IPCC AR4 [*Medhaug and Furevik*, 2011]. The study showed that the models strongly differ in their relationship between AMOCz and sea surface temperature in the North Atlantic, and hence, no consistent mechanism was found to operate across the models.

[59] In IPSLCM4 there is no significant correlation between the WMT_{max} and AMOCσ (Table 3 and gray curve in Figure 16), although the relationship between sea level pressure and AMOCz is found in IPSLCM4 in the study by *Gastineau and Frankignoul* [2011]. The reason for this could be that *Gastineau and Frankignoul* [2011] focus on a larger region, and that the authors identify a correlation related to the model's subtropical heat loss (and not subpolar heat loss). The reason for this difference in IPSLCM4 compared to the other two models could be related to the anomalously cold and fresh surface layer east of Newfoundland (Figure 5). The North Atlantic Current subducts beneath this layer, where its positive sea surface temperature anomalies can be eroded, before it enters the eastern subpolar region. In MPI-M ESM there is also a cold and fresh surface layer east of Newfoundland (Figure 5). However, the more zonal North Atlantic Current in this model (Figure 4) circumvents the cold and fresh surface layer spreading eastward from Newfoundland.

[60] Moving north we investigate the relationship between the northward transport at 60–64°N and the first principal component of AMOCσ. A strengthening of the former is found to lead an increase in AMOCσ in all models (Table 3 and blue curves in Figure 16). The northward transport at 60–64°N represents mainly the Atlantic inflow into the Arctic Mediterranean. This region completes the northern overturning loop, and the consequent dense water mass formation feeds the deep southward branch downstream in the North Atlantic basin [*Dickson and Brown*, 1994; *Rudels et al.*, 1999].

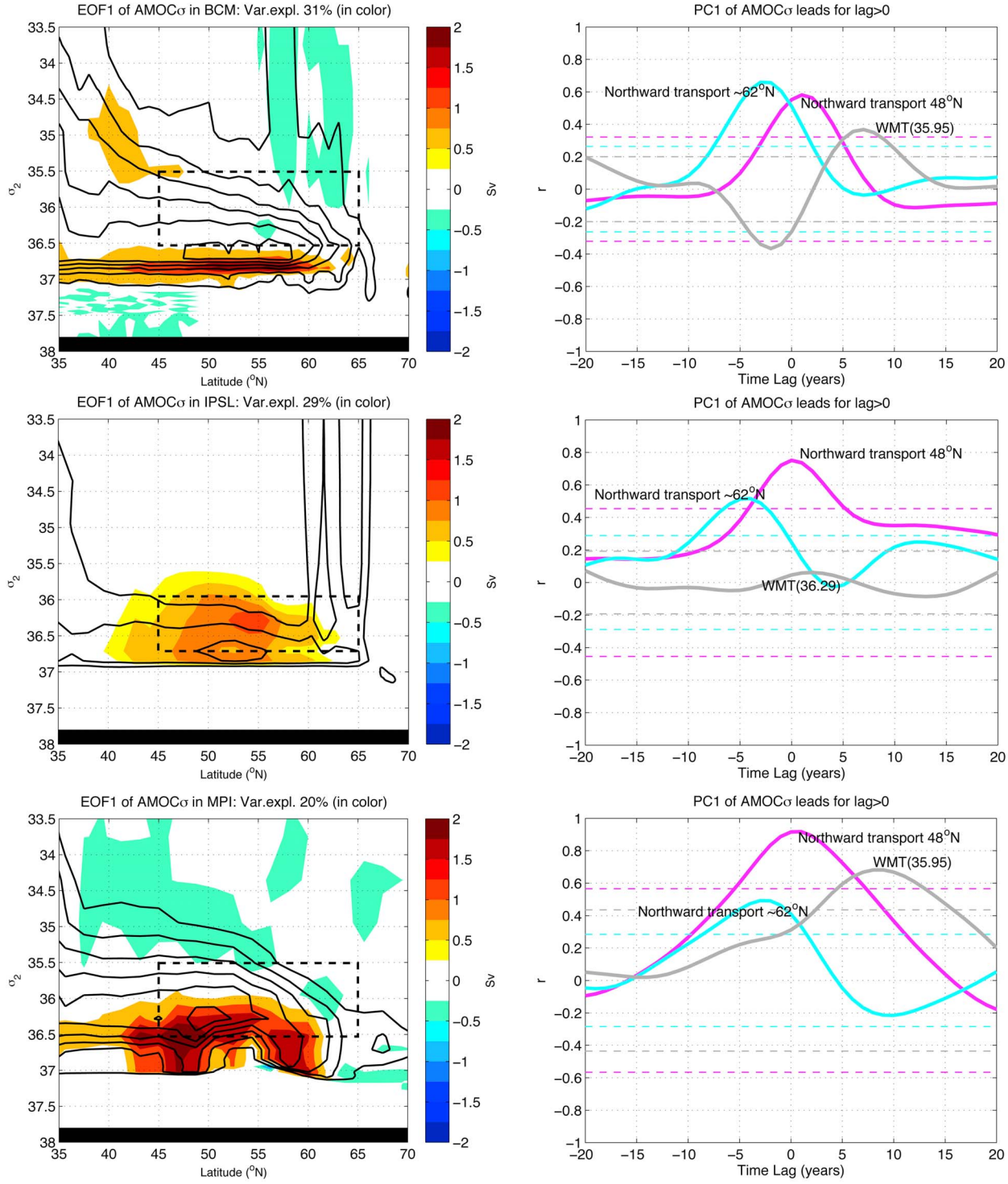

Figure 16. (left) EOF1 of yearly AMOCσ is shown in color for the different models. Model names and the variance explained by EOF1 is indicated in the title of the figures. Mean AMOCσ is shown in contours with intervals of 3 Sv. The dashed rectangles illustrate the density range associated with the surface forced WMT shown in Figures 5–7. (right) Cross-correlation (r) between PC1 of AMOCσ and (1) net northward volume transport at 48°N (magenta), (2) mean net northward transport between 60 and 64°N (blue), and (3) surface forced water mass transformation (WMT) integrated over the eastern subpolar region for the σ_2-densities indicated in the figures (gray). These densities correspond to the maximum WMT for the different models (shown in Figure 3). Positive lags denote the AMOCσ leading, as indicated in the title of the figures. The time series are filtered using a 11-year low-pass filter before the cross-correlation. The dashed lines show 95% significance levels.

Table 2. Northward Volume Transport[a]

	BCM	IPSLCM4	MPI-M ESM
Southern	17.6	8.9	18.9
Northern	9.9	6.8	8.7

[a]The transport (in Sv) is obtained from AMOCσ at the southern (48°N) and northern (60–64°N) boundary of the subpolar region, where the northward flow is integrated over all densities.

[61] The temporal evolution of the northward transport both at 60°–64°N and 48°N is shown in Figure 17. The variance of the northward transport at 60–64°N in MPI-M ESM (std 1 Sv) is almost twice as large as for the other two models (0.6 Sv). Regarding the northward transport at 48°N, the standard deviation for MPI-M ESM is more than three times larger than BCM and IPSLCM4 (1.8 Sv and 0.5 Sv, respectively). The strong variance in the northward flow of MPI-M ESM is reflected in this model's WMT in the eastern subpolar region, which is also higher than in the two other models (Figure 14). The power spectra of the northward transport at 48°N in BCM and IPSLCM4 are also almost following the white noise spectrum (not shown). In contrast, the spectrum for MPI-M ESM shows enhanced energy at 7 and around 50 yrs periodicity. These periods were also found in this model's spectrum of WMT_{max}. Regarding the northward transport at 60–64°N, the spectrum for MPI-M ESM changes, where the energy at (multi)decadal time scales becomes less clearly enhanced (not shown). The spectra for the two other models are comparable to those for the northward transport at 48°N.

[62] The mean ratio of the northward volume transport at 60°–64°N to the northward transport at 48°N is 57%, 76%, and 47% for BCM, IPSLCM4, and MPI-M ESM, respectively. In other words, in BCM and MPI-M ESM about half of the northward flow at 48°N re-circulate in the western subpolar region, while only about a quarter re-circulates in IPSLCM4. The bifurcations of the North Atlantic Current continuing into the Nordic Seas and the Labrador Sea are important for setting the regions of dense water formation, and hence the composition of North Atlantic Deep Water.

[63] The lagged correlations for BCM and MPI-M ESM (Figure 16), demonstrate that an increase in the northward transport at 60°–64°N leads an increase in the southward dense flow in the North Atlantic Basin. Previous studies on the same BCM simulation as used herein, suggest that the atmospheric pattern 'Scandinavian Pattern' is a driver for the variable poleward heat transport across the Greenland-Scotland Ridge [*Medhaug et al.*, 2012]. The poleward heat transport is furthermore positively correlated with both the water mass exchange across the ridge and the AMOCz. This points to atmospheric variability as the link for water mass exchange between the North Atlantic and the Nordic Seas, at least for BCM.

Table 3. Peak Correlations (r) and Corresponding Time Lag in Years[a]

	BCM AMOCσ		IPSLCM4 AMOCσ		MPI-M ESM AMOCσ	
	r	lag	r	lag	r	lag
Northern	0.66	−3	0.52	−4	0.49	−3
Southern	0.58	1	0.75	0	0.92	1
WMT_{max}	−0.37/0.37	−2/7	-	-	0.68	8

[a]The correlations are calculated between the first EOF of AMOCσ and the northward volume transport at the northern (60–64°N) and southern (48°N) boundary of the subpolar region, and the maximum WMT in the eastern subpolar region (WMT_{max}, shown in Figure 14). AMOCσ leads for positive lags. Time series are filtered using a 11-year low-pass filter.

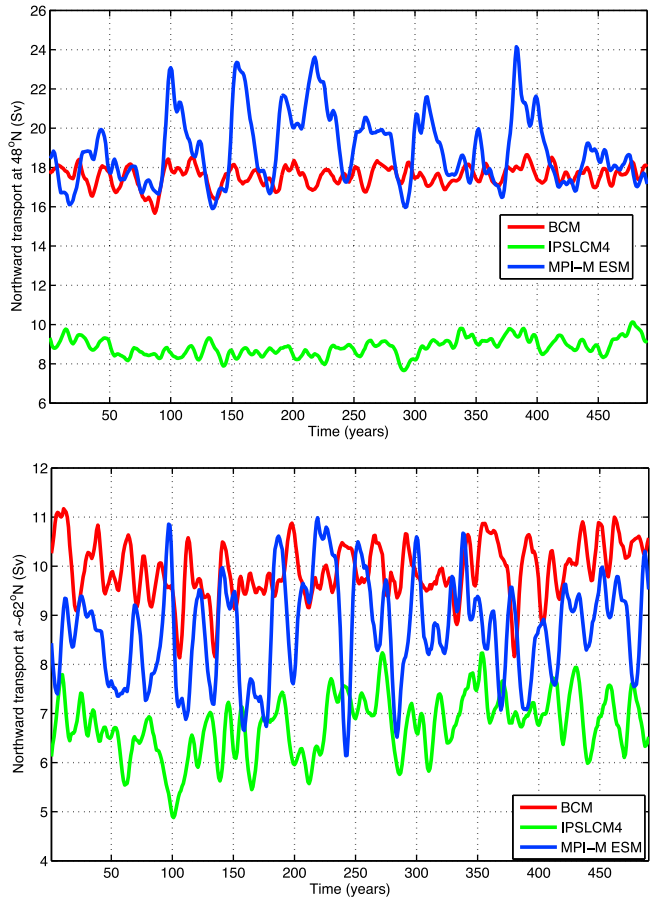

Figure 17. Northward transport at (top) 48°N and (bottom) 60–64°N. The northward transports are the integrated positive volume transport in density space. The time series are filtered using a 11-year low-pass filter.

[64] The northern dense water formation or the subsequent southward dense flow in the North Atlantic Basin is typically found to have a positive correlation with the strength of the AMOCz, i.e., the northward flow, in climate models. This is the case in this study and also in the study mentioned above by *Grist et al.* [2009]. However, this mechanism is not yet fully understood.

6. Conclusions

[65] In this study we have analyzed three 500-yearlong climate model simulations of pre-industrial climate. The focus has been on the mean state and decadal variability of the WMT associated with Subpolar Mode Water and the North Atlantic Current. The model intercomparison of the geographical distribution of the surface forced WMT reveals both similarities and differences. One similarity is that the thermal contribution dominates the WMT in the *eastern* subpolar region, in terms of both the mean state and variability (Figure 10 and Table 1),

and hence, densification of the northward flowing water occurs in this part (Figure 3).

[66] A main objective of the study has been to understand why the surface forced WMT differs among the models. Differences are related to sea ice extent in the Labrador Sea, the relative importance of freshwater close to Newfoundland, and the pathway and intensity of the North Atlantic Current. IPSLCM4 and MPI-M ESM differ from BCM and the observation-based WMT in the Labrador Sea and between Nova Scotia and the eastern subpolar region (Figures 4–7). In IPSLCM4 the barotropic circulation is weaker than in the two other models (Figure 11), its North Atlantic Current subducts at the entrance to the subpolar region, and a quarter of the northward flow at 48°N is estimated to re-circulate in the western subpolar region. The pathway and strength of the North Atlantic Current in IPSLCM4 could be related to the excessive sea ice extent in the Labrador Sea and the excessive fresh water at the surface off Newfoundland (Figure 10). In MPI-M ESM, the North Atlantic Current crosses the entire North Atlantic Basin before continuing north (Figure 11). Even though half of the model's northward flow at 48°N is estimated to re-circulate in the western subpolar region, the heat carried by the current is not sufficient to keep sea ice from advancing south (Figure 10). Hence, similarly to IPSLCM4, the excessive sea ice extent appears closely linked to the pathway of the North Atlantic Current. In summary, identified differences among the models' surface forced WMT can largely be related to aspects of model climatologies that are qualitatively different from what is observed in present climate.

[67] Among the three models, BCM appears to have the more realistic structure of the North Atlantic Current, and the surface forced WMT in BCM is most comparable to the observation-based mean WMT (Figures 4 and 5) [*Brambilla et al.*, 2008]. This is possibly because the model North Atlantic Current joins the Subpolar Gyre directly, without being fragmented into eddies. The observed North Atlantic Current, despite being narrower and more intense in some regions than the model North Atlantic Current, is effectively broadened, slowed and exposed to more surface heat flux by strong eddy activity. No model with such coarse resolution as in this study can truly portray the eddy-rich region connecting Subtropical and Subpolar gyres, and thus the North Atlantic Current will remain a relevant challenge for model development and observational analysis for some time to come. On the other hand, a general implication may be that climate models with a more realistic North Atlantic Current are more appropriate for assessing climatologies and climate change associated with WMT.

[68] Regarding the variable WMT, we found that the decadal variance of surface forced WMT in the eastern subpolar region is reflected by the variance of the poleward flow in the subpolar region. In other words, high variance in oceanic flow is associated with high variance in WMT. A model with high decadal variance in the poleward flow might therefore have stronger communication between ocean and atmosphere close to the European continent. According to *Boer* [2011], MPI-M ESM would appear to have higher decadal potential predictability in the eastern subpolar region, since Boer defines potential predictability as the fraction of the total variance that is accounted for by long time scale components. The three models differ greatly in the intensity and frequency of their natural variability. It is of the greatest importance to create a consistent picture of variability in the decadal frequency band, to distinguish from the human-induced change of climate.

[69] Although the subpolar North Atlantic Ocean is one of the most studied ocean regions, there are still challenges in understanding the variability on decadal timescales both in nature and climate model simulations. Two of the models in this study show an increase in the dense flow *after* a strengthening of the northward flow at the northern boundary of the subpolar region (close to the Greenland-Scotland Ridge), whereas the third model (IPSLCM4) shows an increase in the entire AMOCσ cell (Figure 16). Furthermore, the same two models show an increase in WMT in the eastern subpolar region *after* an increase in the dominant mode of AMOCσ (Figure 16). This relationship is due to intensified heat loss in the eastern subpolar region as a consequence of increased northward flow at the entrance to the subpolar region. An intriguing aspect of the present study is thus that even if climate models are fundamentally different in the climatology of the North Atlantic Ocean, they can appear rather similar in key aspects of decadal variability and zonally averaged AMOCz.

[70] **Acknowledgments.** This work received funding from the European Community's 7th framework program (FP7/2007–2013) under grant agreement GA212643 (Thermohaline Overturning – at Risk (THOR) 2008–2012; HRL, TE, JM, and KL). The Research Council of Norway also provided support through the project IPY-BIAC (HRL and TE). PBR was supported by NASA's Ocean Surface Topography Science Team. This publication is A404 from the Bjerknes Centre for Climate Research. We thank Cecilia M. Bitz for assistance in using the water mass transformation methodology on climate model data. We also thank Iselin Medhaug, Helge Drange, and Odd Helge Otterå for discussions that improved the manuscript.

References

Arhan, M. (1990), The North Atlantic Current and Subarctic Intermediate Water, *J. Mar. Res.*, *48*, 109–144, doi:10.1357/002224090784984605.

Arzel, O., T. Fichefet, and H. Goosse (2006), Sea ice evolution over the 20th and 21st centuries as simulated by current AOGCMs, *Ocean Modell.*, *12*, 401–415, doi:10.1016/j.ocemod.2005.08.002.

Bailey, D. A., P. B. Rhines, and S. Häkkinen (2005), Formation and pathways of North Atlantic Deep Water in a coupled ice-ocean model of the Arctic-North Atlantic Oceans, *Clim. Dyn.*, *25*, 497–516, doi:10.1007/s00382-005-0050-3.

Bentsen, M., H. Drange, T. Furevik, and T. Zhou (2004), Simulated variability of the Atlantic meridional overturning circulation, *Clim. Dyn.*, *22*, 701–720, doi:10.1007/s00382-004-0397-x.

Béranger, K., B. Barnier, S. Gulev, and M. Crépon (2006), Comparing 20 years of precipitation estimates from different sources over the world ocean, *Ocean Dyn.*, *56*, 104–138, doi:10.1007/s10236-006-0065-2.

Bleck, R., C. Rooth, D. Hu, and L. T. Smith (1992), Salinity-driven thermocline transients in a wind- and thermohaline-forced isopycnic coordinate model of the North Atlantic, *J. Phys. Oceanogr.*, *22*, 1486–1505, doi:10.1175/1520-0485(1992)022<1486:SDTTIA>2.0.CO;2.

Boer, G. J. (2011), Decadal potential predictability of twenty-first century climate, *Clim. Dyn.*, *36*, 1119–1133, doi:10.1007/s00382-010-0747-9.

Brambilla, E., and L. D. Talley (2008), Subpolar mode water in the northeastern Atlantic: 1. Averaged properties and mean circulation, *J. Geophys. Res.*, *113*, C04025, doi:10.1029/2006JC004062.

Brambilla, E., L. D. Talley, and P. E. Robbins (2008), Subpolar Mode Water in the northeastern Atlantic: 2. Origin and transformation, *J. Geophys. Res.*, *113*, C04026, doi:10.1029/2006JC004063.

Carman, J. C., and J. L. McClean (2011), Investigation of IPCC AR4 coupled climate model North Atlantic mode water formation, *Ocean Modell.*, *40*, 14–34, doi:10.1016/j.ocemod.2011.07.001.

Cerovečki, I., and J. Marshall (2008), Eddy modulation of air-sea interaction and convection, *J. Phys. Oceanogr.*, *38*, 65–83, doi:10.1175/2007JPO3545.1.

Chelton, D. B. (1983), Effects of sampling errors in statistical estimation, *Deep Sea Res.*, *30*, 1083–1103, doi:10.1016/0198-0149(83)90062-6.

Danabasoglu, G. (2008), On multidecadal variability of the Atlantic Meridional Overturning Circulation in the community climate system model version 3, *J. Clim.*, *21*(21), 5524–5544, doi:10.1175/2008JCLI2019.1.

Deshayes, J., and C. Frankignoul (2008), Simulated variability of the circulation of the North Atlantic from 1953 to 2003, *J. Clim.*, *21*, 4919–4933, doi:11.1175/2008JCLI1882.1.

Dickson, R. R., and J. Brown (1994), The production of North Atlantic Deep Water: Sources, rates and pathways, *J. Geophys. Res.*, *99*, 12,319–12,341, doi:10.1029/94JC00530.

Eden, C., and J. Willebrand (2001), Mechanisms of interannual to decadal variability of the North Atlantic circulation, *J. Clim.*, *14*, 2266–2280, doi:10.1175/1520-0442(2001)014<2266:MOITDV>2.0.CO;2.

Eldevik, T. (2002), On frontal dynamics in two model oceans, *J. Phys. Oceanogr.*, *32*, 2915–2925, doi:10.1175/1520-0485(2002)032<2915:OFDITM>2.0.CO;2.

Enfield, D. B., A. M. Mestaz-Nuñez, and P. J. Trimble (2001), The Atlantic multi-decadal oscillation and its relation to rainfall and river flows in the Continental US, *Geophys. Res. Lett.*, *28*, 2077–2080, doi:10.1029/2000GL012745.

Escudier, R., J. Mignot, and D. Swingedouw (2012), A 20-year coupled ocean-sea ice-atmosphere variability mode in the North Atlantic in an AOGCM, *Clim. Dyn.*, doi:10.1007/s00382-012-1402-4, in press.

Fichefet, T., and A. M. Morales-Maqueda (1997), Sensitivity of a global sea ice model to the treatment of ice thermodynamics and dynamics, *J. Geophys. Res.*, *102*(C6), 12,609–12,646, doi:10.1029/97JC00480.

Fichefet, T., and A. M. Morales-Maqueda (1999), Modelling the influence of snow accumulation and snow-ice formation on the seasonal cycle of the Antarctic sea-ice cover, *Clim. Dyn.*, *15*(4), 251–268, doi:10.1007/s003820050280.

Furevik, T., M. Bentsen, H. Drange, I. K. T. Kindem, N. G. Kvamstø, and A. Sorteberg (2003), Description and validation of the Bergen Climate Model: ARPEGE coupled with MICOM, *Clim. Dyn.*, *21*, 27–51, doi:10.1007/s00382-003-0317-5.

Gastineau, G., and C. Frankignoul (2011), Cold-season atmospheric response to the natural variability in the Atlantic merdional overturning circulation, *Clim. Dyn.*, *39*, 37–57, doi:10.1007/s00382-011-1109-y.

Grist, J. P., and S. A. Josey (2003), Inverse analysis adjustment of the SOC air-sea flux climatology using ocean heat transport constraints, *J. Clim.*, *16*, 3274–3295, doi:10.1175/1520-0442(2003)016<3274:IAAOTS>2.0.CO;2.

Grist, J. P., R. Marsh, and S. A. Josey (2009), On the Relationship between the North Atlantic Meridional Overturning Circulation and the surface forced overturning streamfunction, *J. Clim.*, *22*, 4989–5002, doi:10.1175/2009JCLI2574.1.

Gulev, S. K., B. Barnier, J.-M. Molines, T. Penduff, and J. Chanut (2007), Impact of spatial resolution of simulated surface water mass transformation in the Atlantic, *Ocean Modell.*, *19*, 138–160, doi:10.1016/j.ocemod.2007.07.004.

Häkkinen, S., P. B. Rhines, and D. L. Worthen (2011a), Warm and saline events embedded in the meridional circulation of the northern North Atlantic, *J. Geophys. Res.*, *116*, C03006, doi:10.1029/2010JC006275.

Häkkinen, S., P. B. Rhines, and D. L. Worthen (2011b), Atmospheric blocking and Atlantic multi-decadal ocean variability, *Science*, *334*, 655–659, doi:10.1126/science.1205683.

Hansen, B., and S. Østerhus (2000), North Atlantic-Nordic Seas exchanges, *Prog. Oceanogr.*, *45*, 109–208, doi:10.1016/S0079-6611(99)00052-X.

Hecht, M. W., and R. D. Smith (2008), Toward a physical understanding of the North Atlantic: A review of model studies in an eddying regime, in *Ocean Modeling in an Eddying Regime*, *Geophys. Monogr. Ser.*, vol. 177, edited by M. Hecht and H. Hasumi, pp. 213–239, AGU, Washington, D. C., doi:10.1029/177GM15.

Isachsen, P. E., C. Mauritzen, and H. Svendsen (2007), Dense water formation in the Nordic Seas diagnosed from sea surface buoyancy fluxes, *Deep Sea Res., Part I*, *54*, 22–41, doi:10.1016/j.dsr.2006.09.008.

Johnson, G. C., and N. Gruber (2007), Decadal water mass variations along 20°W in the northeastern Atlantic Ocean, *Prog. Oceanogr.*, *73*, 277–295, doi:10.1016/j.pocean.2006.03.022.

Josey, S. A., E. C. Kent, and P. K. Taylor (1999), New insights into the ocean heat budget closure problem from analysis of the SOC air-sea flux climatology, *J. Clim.*, *12*(9), 2856–2880, doi:10.1175/1520-0442(1999)012<2856:NIITOH>2.0.CO;2.

Josey, S. A., J. P. Grist, and R. Marsh (2009), Estimates of meridional overturning circulation variability in the North Atlantic from surface density flux fields, *J. Geophys. Res.*, *114*, C09022, doi:10.1029/2008JC005230.

Jungclaus, J. H., et al. (2006), Ocean circulation and tropical variability in the coupled model ECHAM5/MPI-OM, *J. Clim.*, *19*(16), 3952–3972, doi:10.1175/JCLI3827.1.

Jungclaus, J. H., et al. (2010), Climate and carbon-cycle variability over the last millennium, *Clim. Past*, *6*, 723–737, doi:10.5194/cp-6-723-2010.

Jungclaus, J. H., H. Haak, M. Latif, and U. Mikolajewicz (2005), Arctic-North Atlantic interactions and multidecadal variability of the meridional overturning circulation, *J. Clim.*, *18*(19), 4013–4031, doi:10.1175/JCLI3462.1.

Kalnay, E., et al. (1996), The NCEP/NCAR 40-year reanalysis project, *Bull. Am. Meteorol. Soc.*, *77*, 437–471, doi:10.1175/1520-0477(1996)077<0437:TNYRP>2.0.CO;2.

Krauss, W. (1986), The North Atlantic Current, *J. Geophys. Res.*, *91*, 5061–5074, doi:10.1029/JC091iC04p05061.

Kwon, Y.-O., and C. Frankignoul (2011), Stochastically-driven multidecadal variability of the Atlantic meridional overturning circulation in CCSM3, *Clim. Dyn.*, *38*, 859–876, doi:10.1007/s00382-011-1040-2.

Langehaug, H. R., I. Medhaug, T. Eldevik, and O. H. Otterå (2012), Arctic/Atlantic exchanges via the subpolar gyre, *J. Clim.*, *25*(7), 2421–2439, doi:10.1175/JCLI-D-11-00085.1.

Large, W. G., and S. G. Yeager (2009), The global climatology of an interannually varying air–sea flux data set, *Clim. Dyn.*, *33*, 341–364, doi:10.1007/s00382-008-0441-3.

Lumpkin, R., and K. Speer (2003), Large-scale vertical and horizontal circulation in the North Atlantic Ocean, *J. Phys. Oceanogr.*, *33*, 1902–1920, doi:10.1175/1520-0485(2003)033<1902:LVAHCI>2.0.CO;2.

Madec, G., P. Delecluse, M. Imbard, and C. Levy (1997), OPA version 8.1 Ocean general circulation model reference manual, *Tech. Rep. 3*, 91 pp., IPSL, Paris.

Manabe, S., and R. J. Stouffer (1988), Two stable equilibria of a coupled ocean-atmosphere model, *J. Clim.*, *1*(9), 841–866, doi:10.1175/1520-0442(1988)001<0841:TSEOAC>2.0.CO;2.

Marsh, R. (2000), Recent variability of the North Atlantic thermohaline circulation inferred from surface heat and freshwater fluxes, *J. Clim.*, *13*, 3239–3260, doi:10.1175/1520-0442(2000)013<3239:RVOTNA>2.0.CO;2.

Marsland, S., H. Haak, J. H. Jungclaus, M. Latif, and F. Röske (2003), The Max Planck Institute global ocean/sea ice model with orthogonal curvilinear coordinates, *Ocean Modell.*, *5*, 91–127, doi:10.1016/S1463-5003(02)00015-X.

Marti, O., et al. (2010), Key features of the IPSL ocean atmosphere model and its sensitivity to atmospheric resolution, *Clim. Dyn.*, *34*, 1–26, doi:10.1007/s00382-009-0640-6.

Mauritzen, C., and S. Häkkinen (1999), On the relationship between dense water formation and the "Meridional Overturning Cell" in the North Atlantic Ocean, *Deep Sea Res., Part I*, *46*, 877–894, doi:10.1016/S0967-0637(98)00094-6.

McCartney, M. S., and L. D. Talley (1982), The Subpolar Mode Water of the North Atlantic, *J. Phys. Oceanogr.*, *12*, 1169–1188, doi:10.1175/1520-0485(1982)012<1169:TSMWOT>2.0.CO;2.

McDougall, T. J. (1987), Neutral surfaces, *J. Phys. Oceanogr.*, *17*, 1950–1964, doi:10.1175/1520-0485(1987)017<1950:NS>2.0.CO;2.

Medhaug, I., and T. Furevik (2011), North Atlantic 20th century multidecadal variability in coupled climate models: Sea surface temperature and ocean overturning circulation, *Ocean Sci.*, *7*, 389–404, doi:10.5194/os-7-389-2011.

Medhaug, I., H. R. Langehaug, T. Eldevik, T. Furevik, and M. Bentsen (2012), Mechanisms for decadal scale variability in a simulated Atlantic meridional overturning circulation, *Clim. Dyn.*, *39*(1–2), 77–93, doi:10.1007/s00382-011-1124-z.

Mignot, J., and C. Frankignoul (2010), Local and remote impacts of a tropical Atlantic salinity anomaly, *Clim. Dyn.*, *35*(7–8), 1133–1147, doi:10.1007/s00382-009-0621-9.

Nurser, A. J. G., R. Marsh, and R. G. Williams (1999), Diagnosing water mass formation from air-sea fluxes and surface mixing, *J. Phys. Oceanogr.*, *29*, 1468–1487, doi:10.1175/1520-0485(1999)029<1468:DWMFFA>2.0.CO;2.

Old, C., and K. Haines (2006), North Atlantic Subtropical Mode Water and ocean memory in HadCM3, *J. Clim.*, *19*, 1126–1148, doi:10.1175/JCLI3650.1.

Østerhus, S., W. R. Turrell, S. Jónsson, and B. Hansen (2005), Measured volume, heat, and salt fluxes from the Atlantic to the Arctic Mediterranean, *Geophys. Res. Lett.*, *32*, L07603, doi:10.1029/2004GL022188.

Otterå, O. H., M. Bentsen, I. Bethke, and N. G. Kvamstø (2009), Simulated pre-industrial climate in Bergen Climate Model (version 2): Model description and large-scale circulation features, *Geosci. Model. Dev.*, *2*, 197–212, doi:10.5194/gmd-2-197-2009.

Pérez-Brunius, P., T. Rossby, and D. R. Watts (2004), Transformation of the warm waters of the North Atlantic from a geostrophic streamfunction perspective, *J. Phys. Oceanogr.*, *34*, 2238–2256, doi:10.1175/1520-0485(2004)034<2238:TOTWWO>2.0.CO;2.

Rahmstorf, S. (2002), Ocean circulation and climate during the past 120,000 years, *Nature*, *419*, 207–214, doi:10.1038/nature01090.

Reverdin, G. (2010), North Atlantic subpolar gyre surface variability (1895–2009), *J. Clim.*, *23*, 4571–4584, doi:10.1175/2010JCLI3493.1.

Rhines, P., S. Häkkinen, and S. A. Josey (2008), Is oceanic heat transport significant in the climate system?, in *Arctic-Subarctic Ocean Fluxes: Defining the Role of the Northern Seas in Climate*, edited by B. Dickson, J. Meincke, and P. Rhines, pp. 87–109, Springer, Dordrecht, Netherlands, doi:10.1007/978-1-4020-6774-7_5.

Röske, F. (2006), A global heat and freshwater forcing dataset for ocean models, *Ocean Modell.*, *11*, 235–297, doi:10.1016/j.ocemod.2004.12.005.

Rossby, T. (1996), The North Atlantic Current and surrounding waters: At the crossroads, *Rev. Geophys.*, *34*, 463–481, doi:10.1029/96RG02214.

Roullet, G., and G. Madec (2000), Salt conservation, free surface, and varying levels: A new formulation for ocean general circulation models, *J. Geophys. Res.*, *105*(C10), 23,927–23,942, doi:10.1029/2000JC900089.

Rudels, B., H. J. Friedrich, and D. Quadfasel (1999), The Arctic Circumpolar Boundary Current, *Deep Sea Res., Part II*, *46*, 1023–1062, doi:10.1016/S0967-0645(99)00015-6.

Salas Mélia, D. (2002), A global coupled sea ice-ocean model, *Ocean Modell.*, *4*, 137–172, doi:10.1016/S1463-5003(01)00015-4.

Schmitz, W., and M. McCartney (1993), On the North Atlantic circulation, *Rev. Geophys.*, *31*(1), 29–49, doi:10.1029/92RG02583.

Servonnat, J., P. Yiou, M. Khodri, D. Swingedouw, and S. Denvil (2010), Influence of solar variability, CO_2 and orbital forcing during the last millennium in the IPSLCM4 model, *Clim. Past*, *6*, 445–460, doi:10.5194/cp-6-445-2010.

Smethie, W. M., and R. A. Fine (2001), Rates of North Atlantic Deep Water formation calculated from chlorofluorocarbon inventories, *Deep Sea Res., Part I*, *48*, 189–215, doi:10.1016/S0967-0637(00)00048-0.

Speer, K., and E. Tziperman (1992), Rates of water mass formation in the North Atlantic Ocean, *J. Phys. Oceanogr.*, *22*, 93–104, doi:10.1175/1520-0485(1992)022<0093:ROWMFI>2.0.CO;2.

Swift, J. H. (1986), The Arctic waters, in *The Nordic Seas*, edited by B. G. Hurdle, pp. 129–154, Springer, New York, doi:10.1007/978-1-4615-8035-5_5.

Swingedouw, D., P. Braconnot, P. Delecluse, E. Guilyardi, and O. Marti (2007), The impact of global freshwater forcing on the thermohaline circulation: Adjustment of North Atlantic convection sites in a CGCM, *Clim. Dyn.*, *28*, 291–305, doi:10.1007/s00382-006-0171-3.

Talley, L. D., J. L. Reid, and P. E. Robbins (2003), Data-based meridional overturning streamfunctions for the global ocean, *J. Clim.*, *16*, 3213–3226, doi:10.1175/1520-0442(2003)016<3213:DMOSFT>2.0.CO;2.

Tandon, A., and L. Zhao (2004), Mixed layer transformation for the North Atlantic for 1990–2000, *J. Geophys. Res.*, *109*, C05018, doi:10.1029/2003JC002059.

Thierry, V., E. de Boisséson, and H. Mercier (2008), Interannual variability of the Subpolar Mode Water properties over the Reykjanes Ridge during 1990–2006, *J. Geophys. Res.*, *113*, C04016, doi:10.1029/2007JC004443.

Trenberth, K. E., and J. M. Caron (2001), Estimates of meridional atmosphere and ocean heat transports, *J. Clim.*, *14*, 3433–3443, doi:10.1175/1520-0442(2001)014<3433:EOMAAO>2.0.CO;2.

Walin, G. (1982), On the relation between sea-surface heat flow and thermal circulation in the ocean, *Tellus*, *34*, 187–195, doi:10.1111/j.2153-3490.1982.tb01806.x.

Willebrand, J., et al. (2001), Circulation characteristics in three eddy-permitting models of the North Atlantic, *Prog. Oceanogr.*, *48*, 123–161, doi:10.1016/S0079-6611(01)00003-9.

Zhang, R. (2010), Latitudinal dependence of Atlantic meridional overturning circulation (AMOC) variations, *Geophys. Res. Lett.*, *37*, L16703, doi:10.1029/2010GL044474.

Zhu, X., and J. Jungclaus (2008), Interdecadal variability of the meridional overturning circulation as an ocean internal mode, *Clim. Dyn.*, *31*, 731–741, doi:10.1007/s00382-008-0383-9.